FIG. 21. The average diffusivity $< \xi^2 \omega_a >$, averaged over the range $0.04 < \epsilon < 0.2$, as a function of Ω.
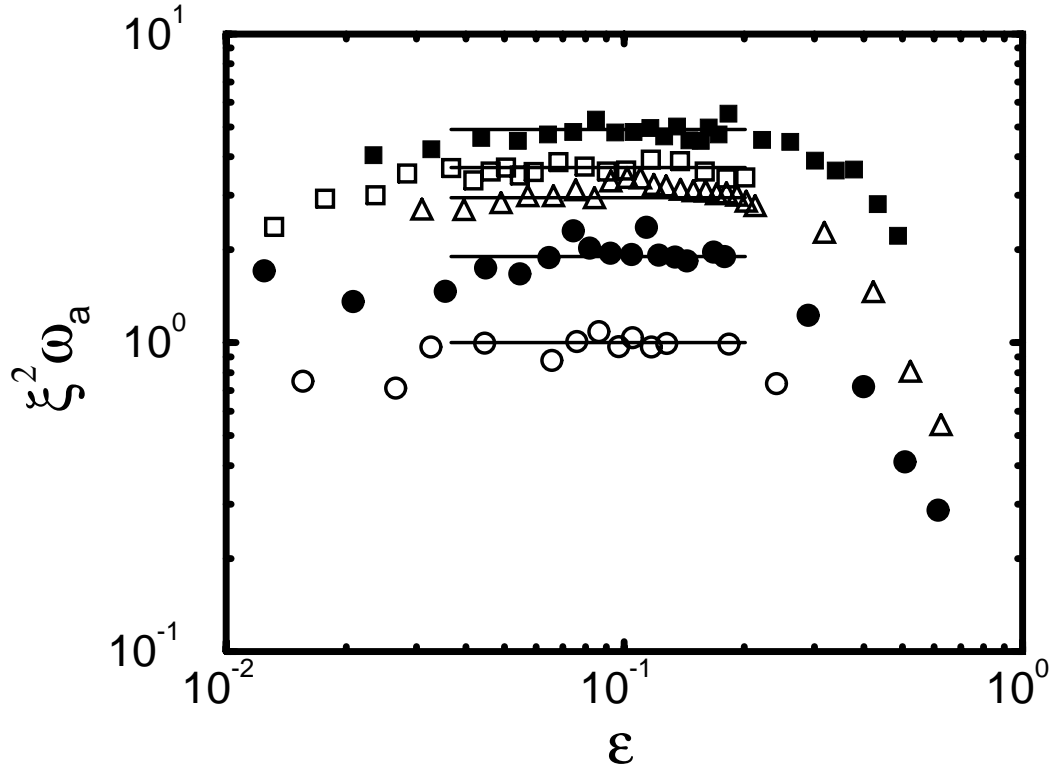
FIG. 20. The diffusivity $D = \xi^2 \omega_a$ as a function of ϵ for $\Omega = 12.6$ (open circles), $\Omega = 14.3$ (solid circles), $\Omega = 16.5$ (open triangles), $\Omega = 17.6$ (open squares), and $\Omega = 19.8$ (solid squares). The solid lines are averages $< \xi^2 \omega_a >$ of the data for a given Ω for $0.04 < \epsilon < 0.2$.
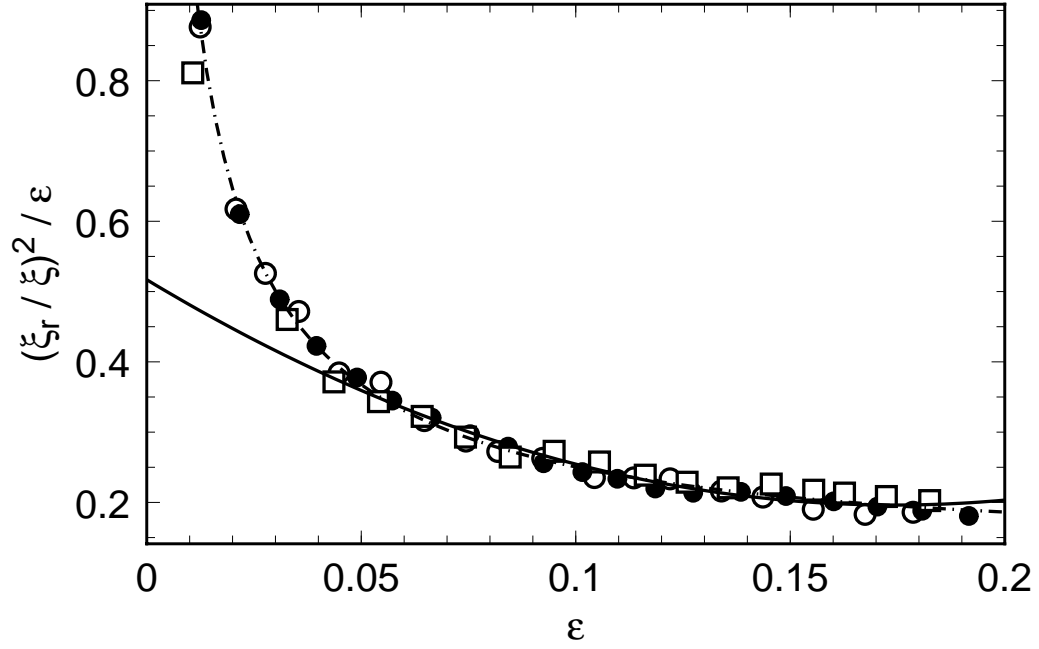
FIG. 19. The inverse square $(1/\tilde{\xi})^2$ of the reduced correlation length $\tilde{\xi} = \xi/\xi_r$, divided by ϵ, as a function of ϵ on linear scales. The data are for $(\Omega, \xi_r) = (14.3, 1.00)$ (open circles), $(16.5, 0.913)$ (solid circles), and $(19.7, 0.839)$ (open squares). The dash-dotted line is a fit of the power law Eq. 8 to the data and corresponds to an exponent of 0.17. The solid line is a fit of Eq. 9 to the data.

FIG. 18. The reduced correlation length $\tilde{\xi} = \xi/\xi_r$ as a function of ϵ on logarithmic scales. The data are for $(\Omega, \xi_r) = (14.3, 1.00)$ (open circles), $(16.5, 0.913)$ (solid circles), and $(19.7, 0.839)$ (open squares). The dash-dotted line is a fit of the powerlaw Eq. 8 to the data and corresponds to an exponent of 0.17. The solid line is a fit of Eq. 9 to the data.
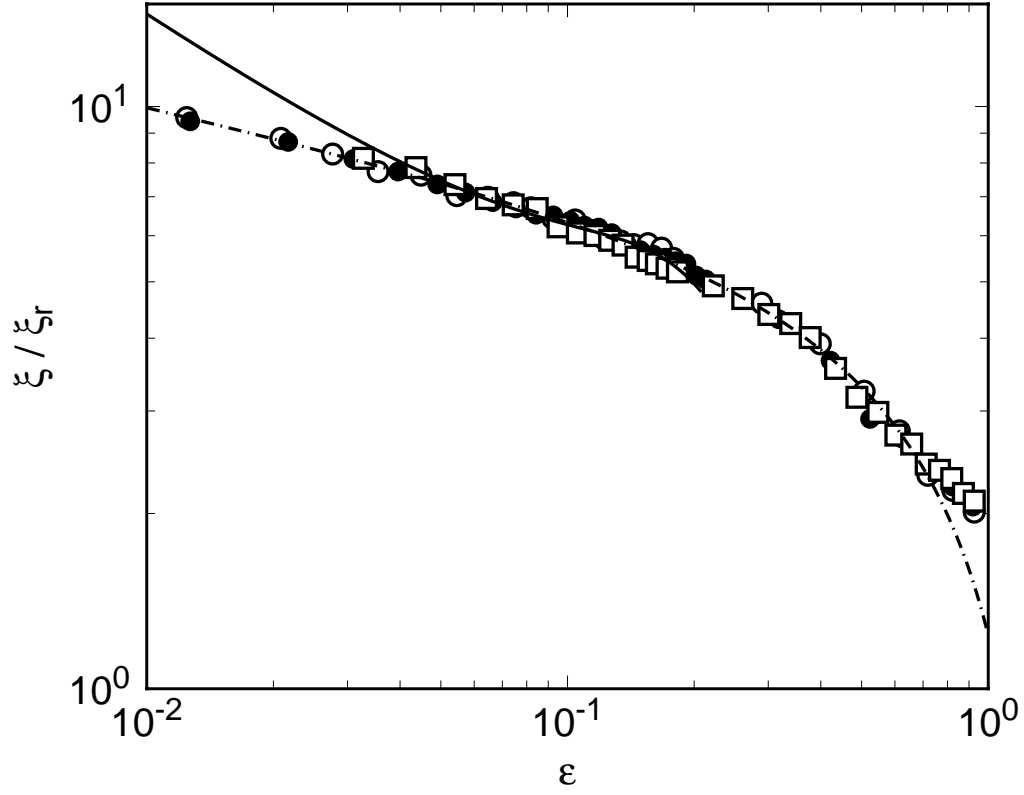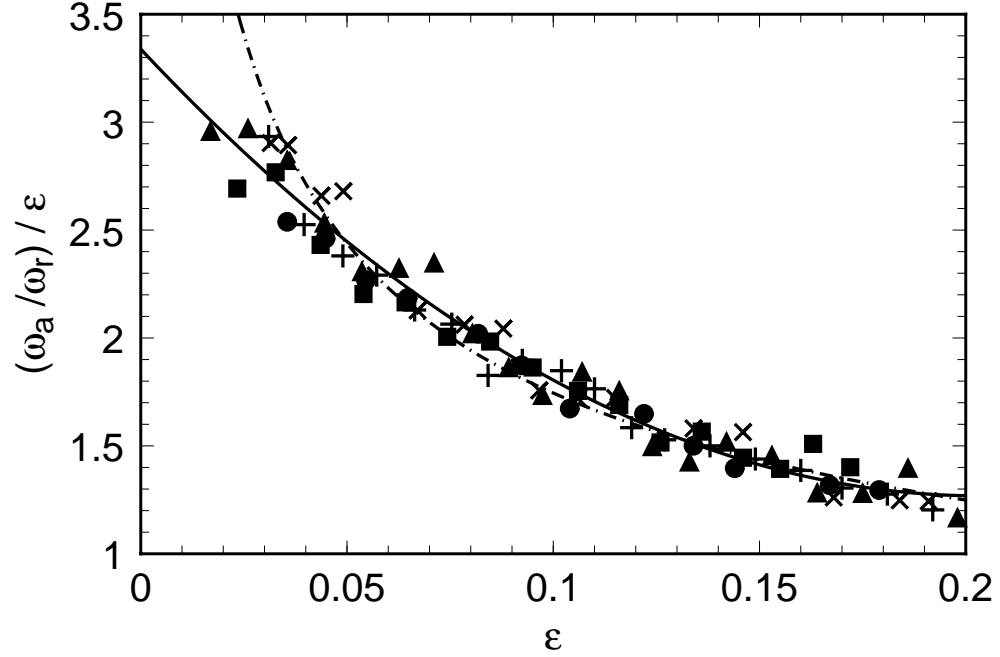
FIG. 17. The reduced frequency $\tilde{\omega}_a = \omega_a/\omega_r$ divided by ϵ as a function of ϵ on linear scales. The data are for $(\Omega, \omega_r) = (13.2, 0.152)$ (crosses), $(14.3, 0.273)$ (circles), $(15.3, 0.400)$ (triangles), $(16.5, 0.541)$ (plusses), and $(19.8, 1.000)$ (squares).The solid line is a fit of Eq. 6 to the data. The dash-dotted line is a fit of the power-law Eq. 5 to the data and corresponds to an exponent of 0.52.
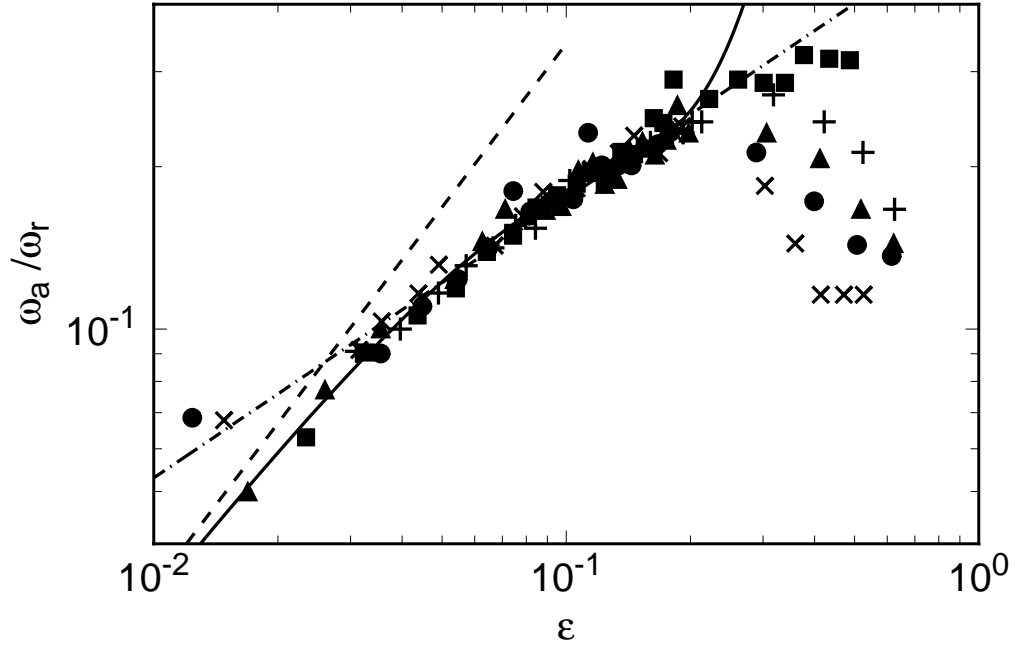
FIG. 16. The reduced frequency $\tilde{\omega}_a = \omega_a/\omega_r$ as a function of ϵ for $, = 40$ on logarithmic scales. The data are for $(\Omega, \omega_r) = (13.2, 0.152)$ (crosses), $(14.3, 0.273)$ (circles), $(15.3, 0.400)$ (triangles), $(16.5, 0.541)$ (plusses), and $(19.8, 1.000)$ (squares). The dashed line corresponds to an exponent of one. The dash-dotted line is a fit of the powerlaw Eq. 5 to the data and corresponds to an exponent of 0.52. The solid line is a fit of Eq. 6 to the data.
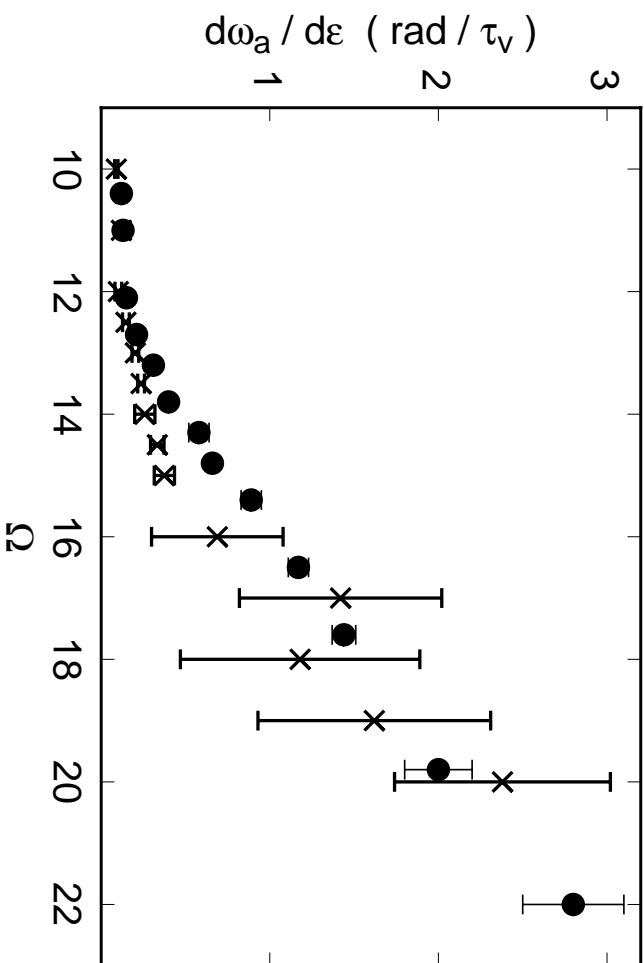
FIG. 15. The slope $W = d\omega_a/d\epsilon$ for small ϵ as a function of Ω for , $= 40$, $\sigma = 0.93$ (solid circles) and , $= 23$, $\sigma = 0.83$ (crosses).
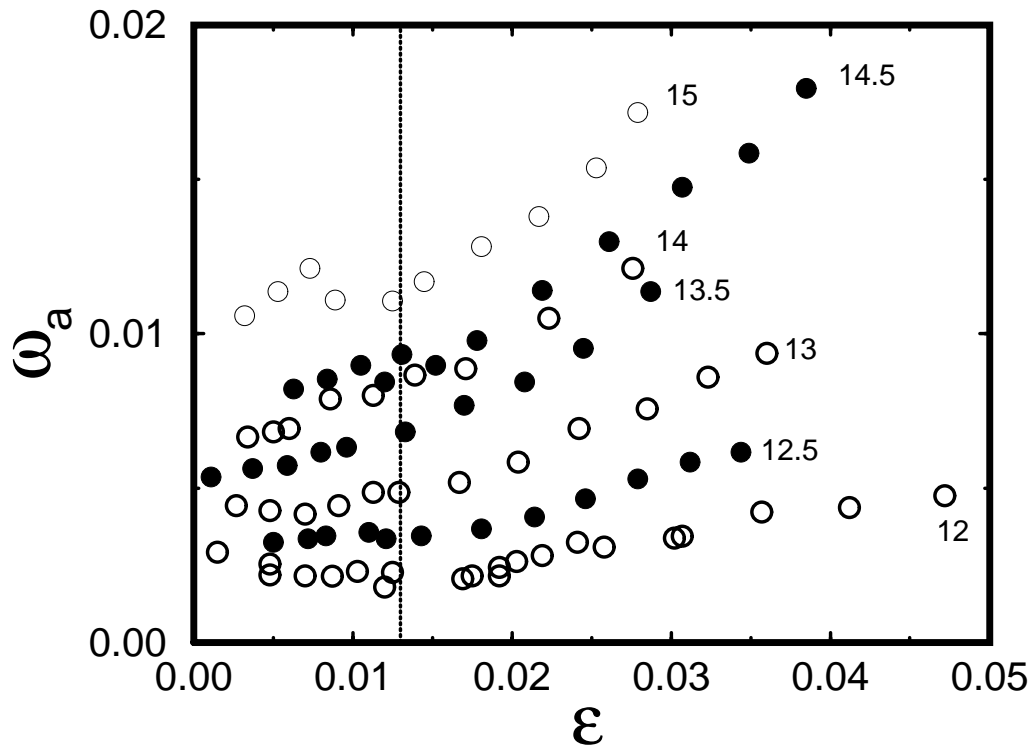
FIG. 14. The frequency ω_a as a function of ϵ for , $= 23$ and the Ω values given in the figure.
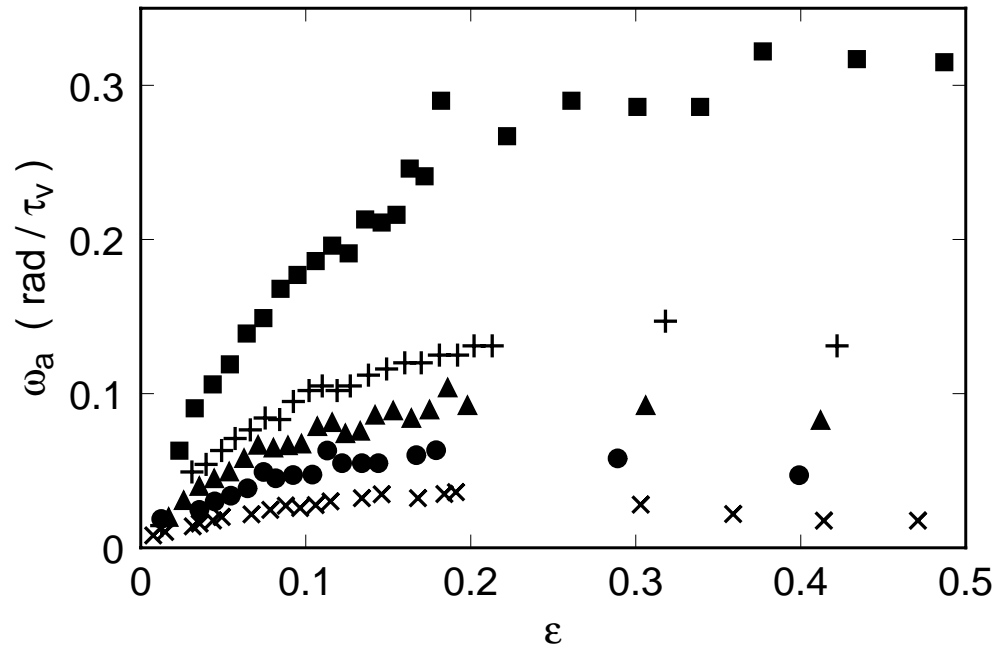
FIG. 13. The frequency ω_a as a function of ϵ for , $= 40$ and $\Omega = 13.2$ (crosses), 14.3 (circles), 15.3 (triangles), 16.5 (plusses), and 19.8 (squares).
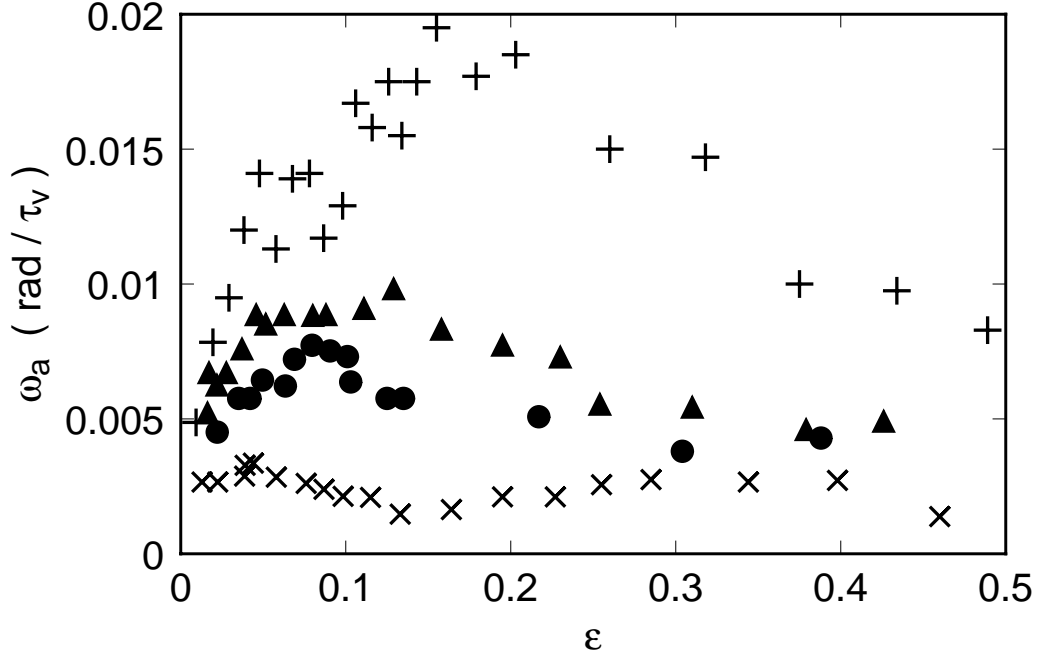
FIG. 12. The frequency ω_a as a function of ϵ for $, = 40$ and $\Omega = 8.8$ (crosses), 10.5 (circles), 11.0 (triangles) and 12.1 (plusses).
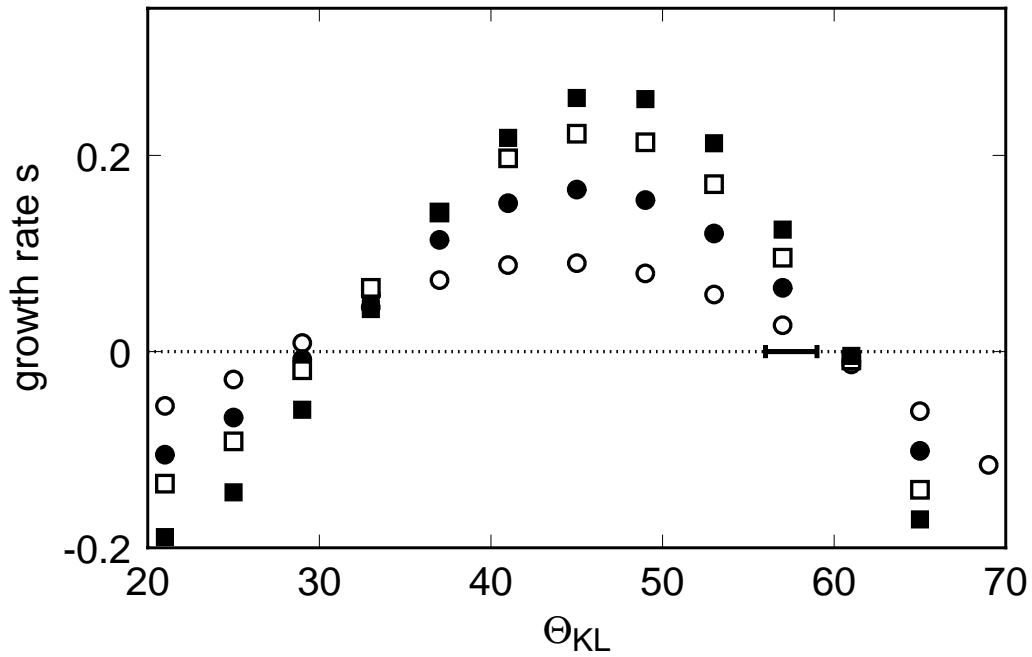
FIG. 11. Calculated growth rates $s(\Theta_{KL})$ as a function of Θ_{KL} for $\Omega = 15.4$ and $\epsilon = 0.05$ (open circles), 0.10 (solid circles), 0.15 (open squares), and 0.20 (solid squares). The small horizontal bar represents the experimental results for Θ_s shown in Fig. 10.
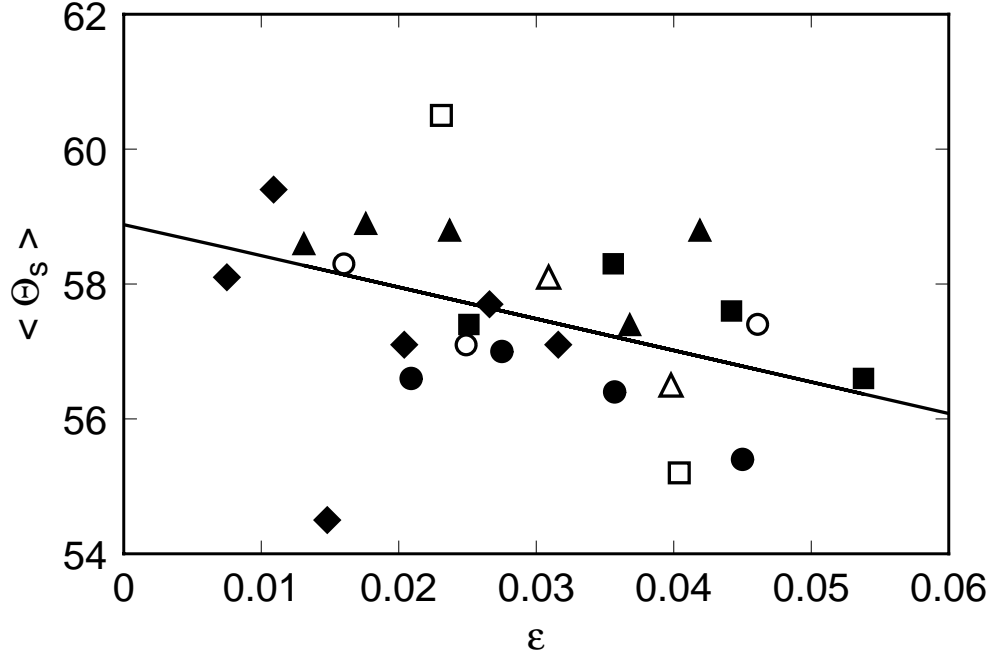
FIG. 10. Measured switching angle $< \Theta_s >$ for , $= 40$ as a function of ϵ for $\Omega = 13.2$ (solid diamonds), 13.8 (open circles), 14.3 (solid circles), 14.9 (open squares), 15.4 (solid squares), 16.5 (open triangles), and 17.6 (solid triangles).
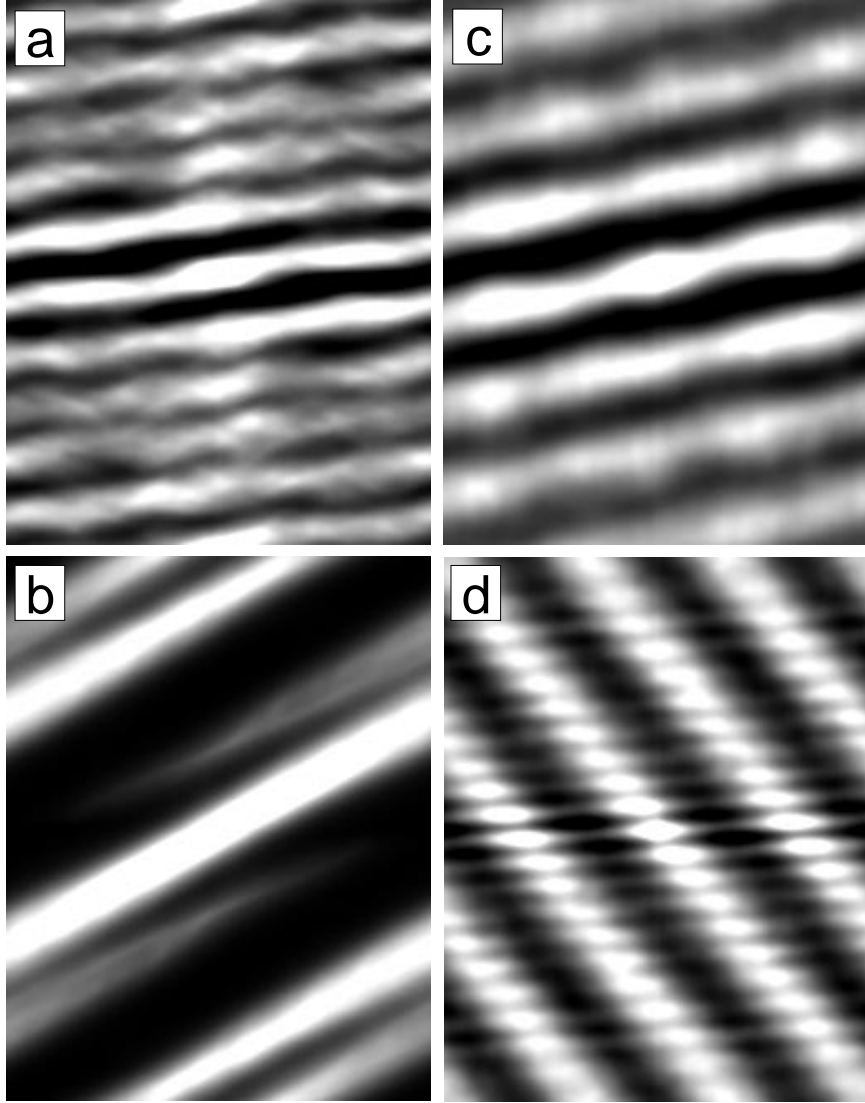
FIG. 9. Grey-scaled auto-correlations $C(\delta\Theta, \delta t)$ for the angle-time plots in Fig. 8. (a): $\Omega = 8.8, \epsilon = 0.04$. (b): $\Omega = 8.8, \epsilon = 0.16$. (c): $\Omega = 12.7, \epsilon = 0.10$. (d): $\Omega = 16.5, \epsilon = 0.03$. Bright (dark) corresponds to large (small) values.
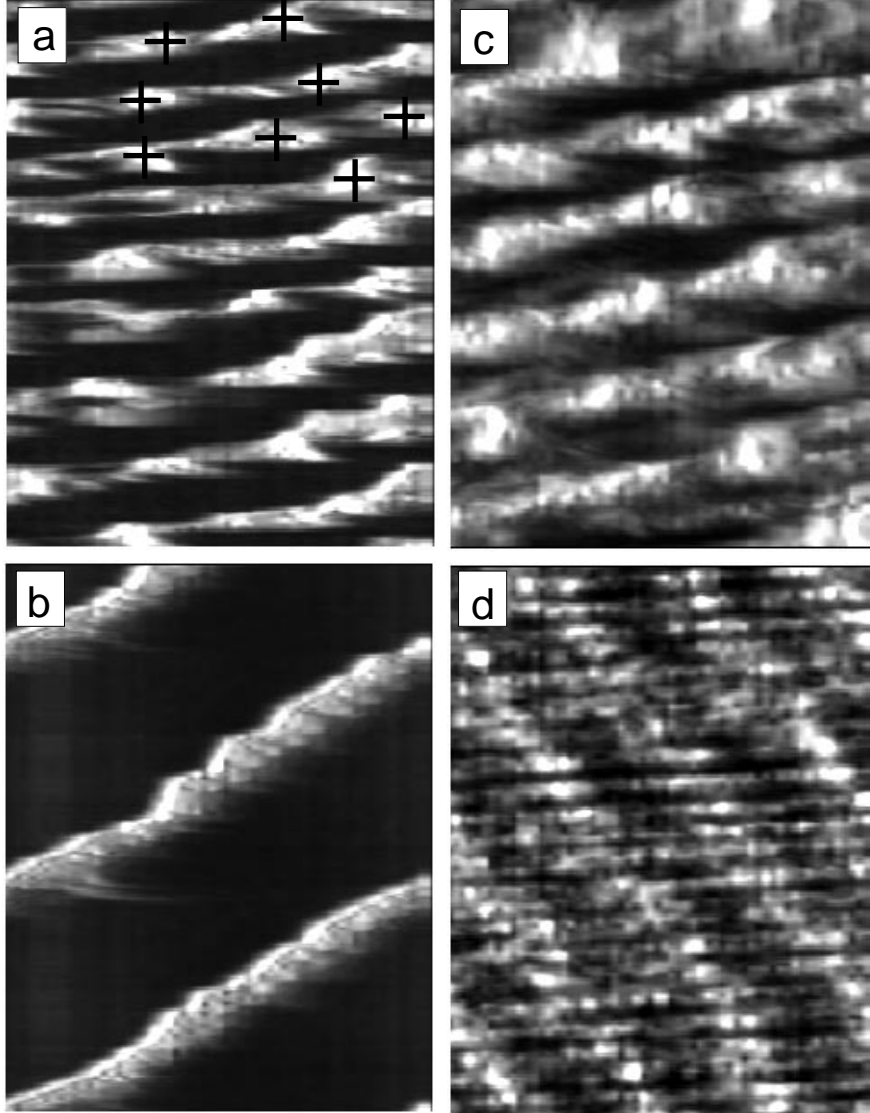
FIG. 8. Grey-scaled angle-time plots of $S(\Theta, t)$ for $, = 40$ and (a) $\Omega = 8.8$, $\epsilon = 0.04$, $9600\tau_v$, (b) $\Omega = 8.8$, $\epsilon = 0.16$, $4800\tau_v$, (c) $\Omega = 12.7$, $\epsilon = 0.10$, $1133\tau_v$, and (d) $\Omega = 16.5$, $\epsilon = 0.03$, $1600\tau_v$. Bright (dark) corresponds to large (small) values.
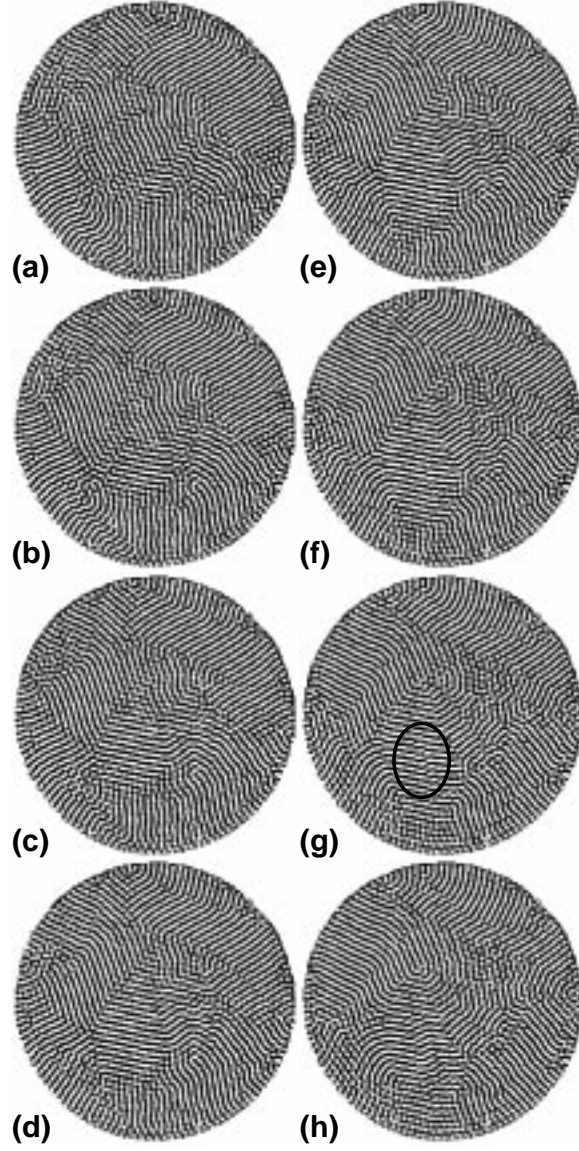
FIG. 7. Time sequence of images for , = 40 with Küppers-Lortz domains and dislocation-defect motion at $\epsilon = 0.03$ and $\Omega = 16.5$. The images are 6.7 τ_v apart. The ellipse in (g) contains a pair of defects which formed by the pinching-off of a roll.
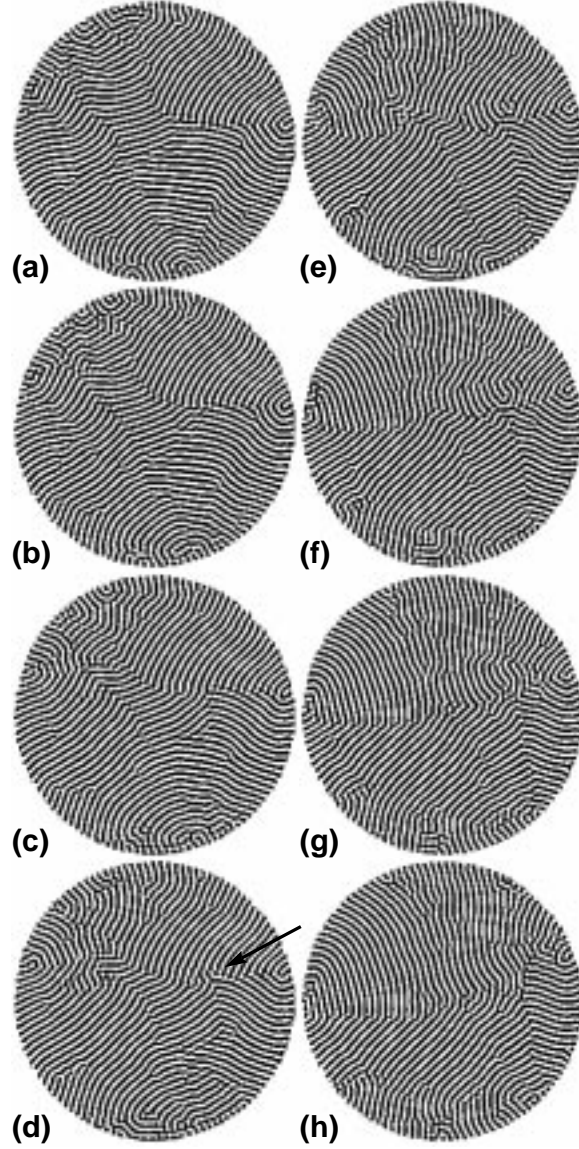
FIG. 6. Time sequence of images for , = 40 with Küppers-Lortz domains and dislocation-defect motion at $\epsilon = 0.10$ and $\Omega = 12.7$. The images are 8.9 τ_v apart. The arrow in (d) points to a region away from the sidewall with a spontaneously-nucleated domain wall.
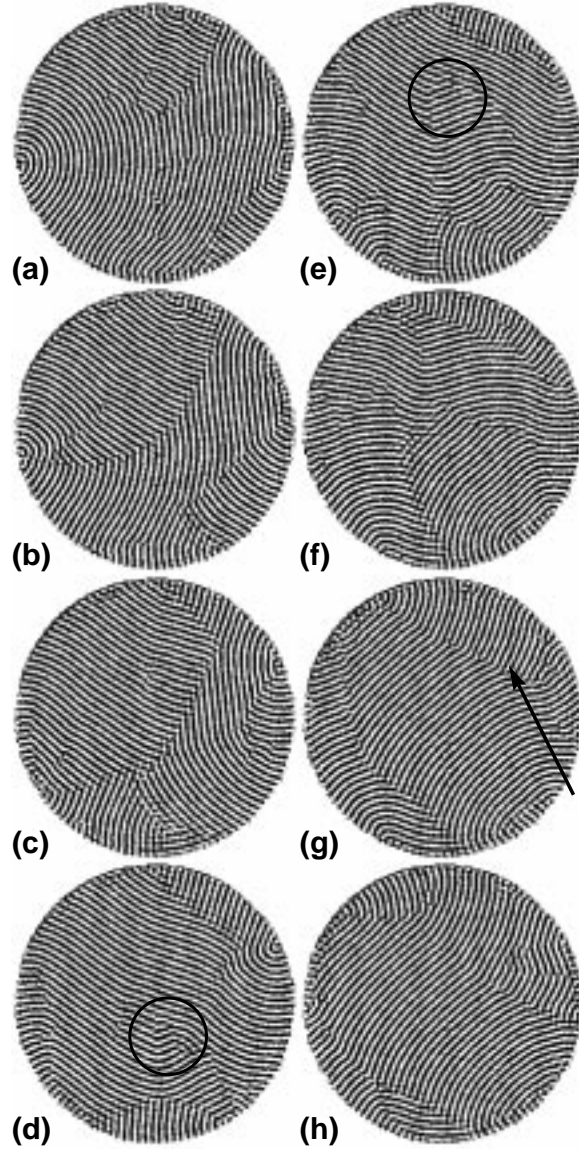
FIG. 5. Time sequence of images for , = 40 with sidewall-nucleated Küppers-Lortz domains and dislocation-defect motion at $\epsilon = 0.04$ and $\Omega = 8.8$. The images are 80 τ_v apart.
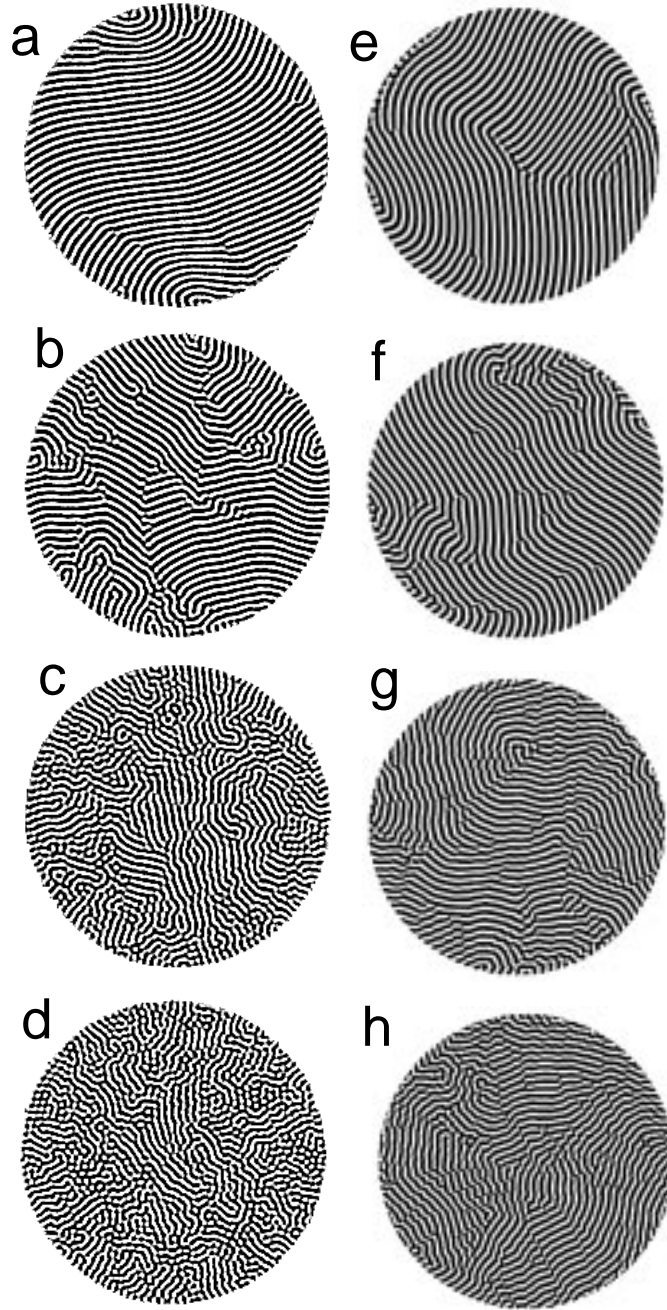
FIG. 4. Representative patterns for , = 40 from experiment (left) and from integrations of the Boussinesq equations (right). (a, e): $\Omega = 8.8$, $\epsilon = 0.16$. (b, f): $\Omega = 12.7$, $\epsilon = 0.18$. (c, g): $\Omega = 16.5$, $\epsilon = 0.16$. (d, h): $\Omega = 19.8$, $\epsilon = 0.18$.
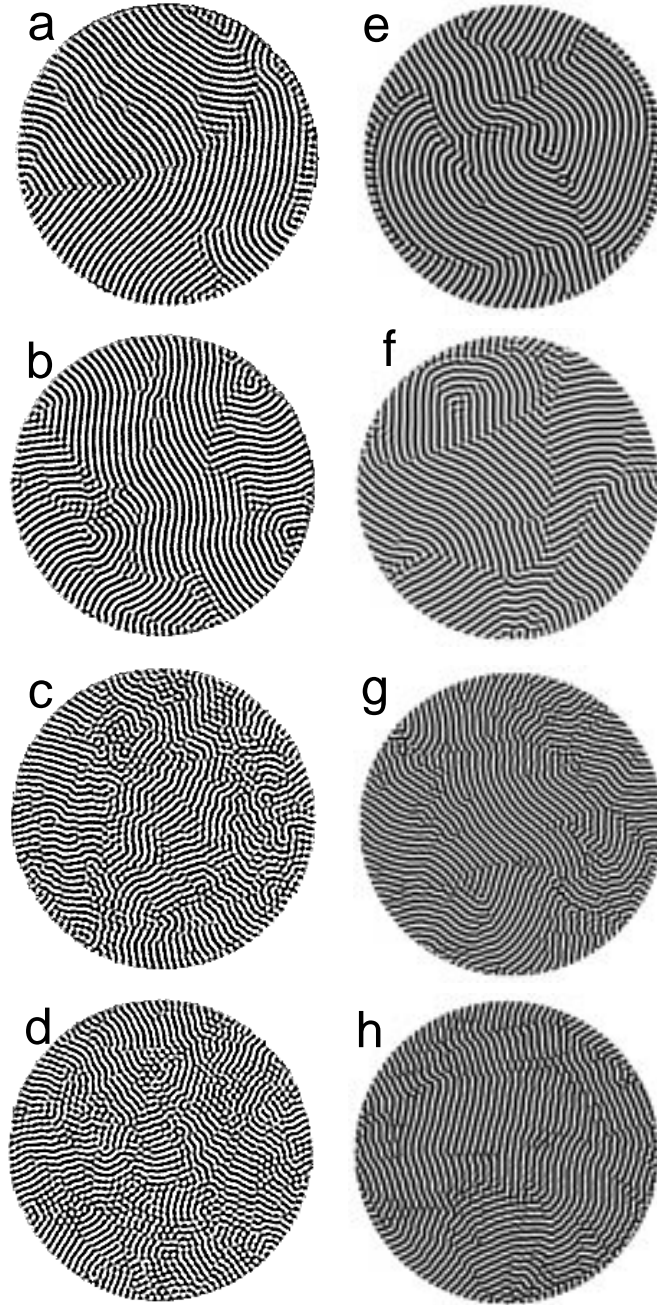
FIG. 3. Representative patterns for , = 40 from experiment (left) and from integrations of the Boussinesq equations (right) at $\epsilon = 0.06$ for (a, e) $\Omega = 8.8$, (b, f) $\Omega = 12.7$, (c, g) $\Omega = 16.5$, and (d, h) $\Omega = 19.8$.
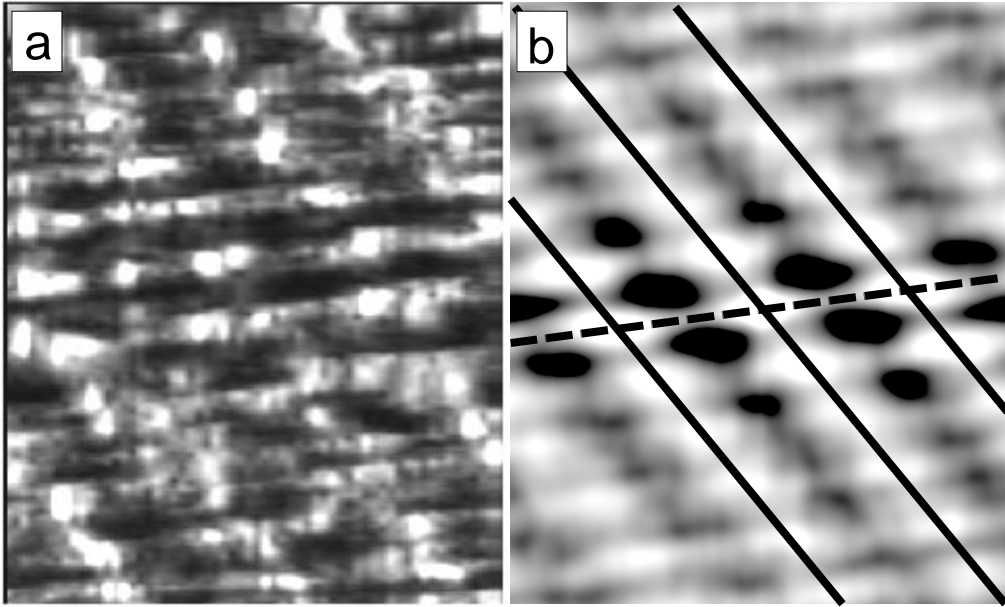
FIG. 2. An example of (a) $F(\Theta, t)$ and (b) $C(\delta\Theta, \delta t)$ for $\Omega = 15.4$ and $\epsilon = 0.027$. For $F(\Theta, t)$ the horizontal axis spans $0 < \Theta < \pi$. The vertical axis for t covers an interval of $2080\tau_v$, with t increasing in the upward direction. For $C(\delta\Theta, \delta t)$ the origin is in the center, with $-\pi/2 < \delta\Theta < \pi/2$ and $-1040 < \delta t < 1040$. Bright (dark) are high (low) values.
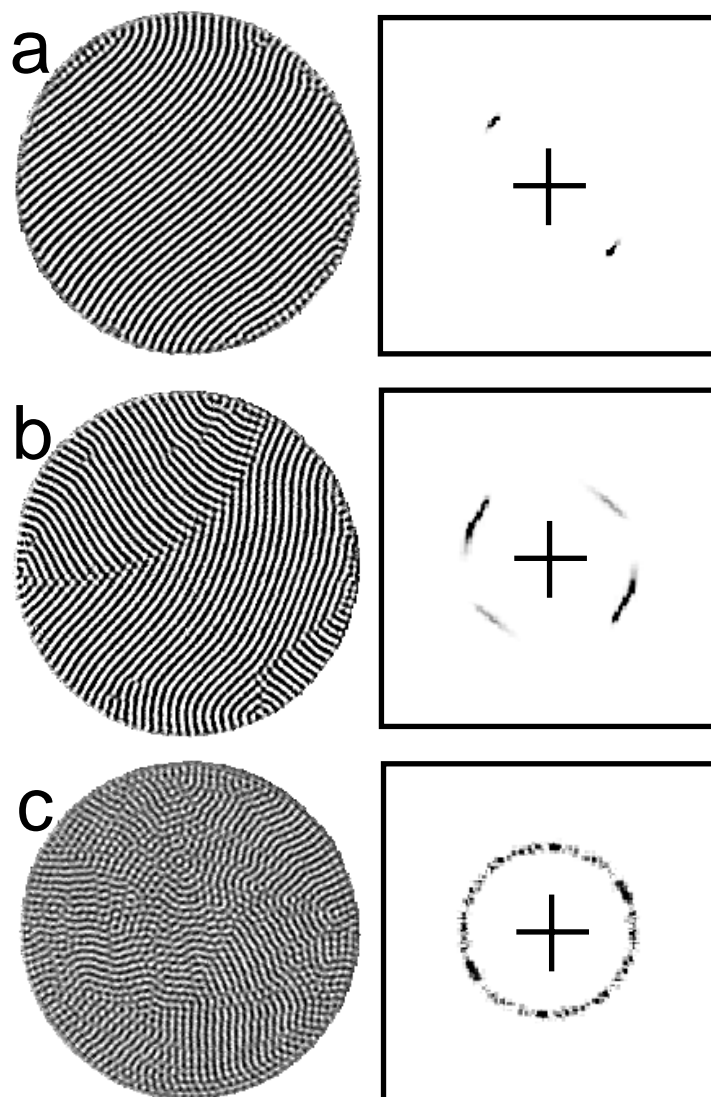
FIG. 1. Real-space images and their grey-scaled Fourier-transform moduli $F(\mathbf{k}, t)$ for (a) $\Omega = 4.4$ and $\epsilon = 0.05$, (b) $\Omega = 8.8$ and $\epsilon = 0.05$, and (c) $\Omega = 17.6$ and $\epsilon = 0.024$.

Press, Oxford, 1961).

[20] K. E. Heikes, Ph.D. thesis, University of California, Los Angeles, 1979.

[21] Y. Hu, R. E. Ecke, and G. Ahlers, Phys. Rev. E **55**, 6928 (1997).

[22] T. Clune and E. Knobloch, Phys. Rev. E **47**, 2536 (1993).

[23] R. M. May and W. J. Leonard, SIAM J. Appl. Math. **29**, 243 (1975).

[24] J. Swift and P. Hohenberg, Phys. Rev. A **15**, 319 (1977).

[25] M. Bestehorn, M. Fantz, R. Friedrich, and H. Haken, Phys. Lett. A **174**, 48 (1993).

[26] J. M. Rodríquez, C. Perez-Garcia, M. Bestehorn, M. Neufeld, and R. Friedrich, Chaos **4**, 369 (1994).

[27] J. M. Rodríquez, C. Perez-Garcia, M. Bestehorn, M. Neufeld, and R. Friedrich, Phys. Rev. Lett. **74**, 530 (1995).

[28] S. W. Morris, E. Bodenschatz, D. S. Cannell, and G. Ahlers, Phys. Rev. Lett. **71**, 2026 (1993).

[29] Y. Hu, R. E. Ecke, and G. Ahlers, Phys. Rev. E **48**, 4399 (1993).

[30] J. R. de Bruyn, E. Bodenschatz, S. W. Morris, S. Trainoff, Y. Hu, D. S. Cannell, and G. Ahlers, Rev. Sci. Instrum. **67**, 2043 (1996).

[31] Y. Hu, Ph.D. thesis, University of California, Santa Barbara, 1995.

[32] Y. Hu, R. E. Ecke, and G. Ahlers, Phys. Rev. E **51**, 3263 (1995).

[33] W. Decker, W. Pesch, and A. Weber, Phys. Rev. Lett. **73**, 648 (1994).

[34] W. Pesch, Chaos **6**, 348 (1996).

[35] D. Egolf, V. Melnikov, and E. Bodenschatz, Phys. Rev. Lett. **80**, 3228 (1998).

REFERENCES

[1] G. Küppers and D. Lortz, J. Fluid Mech. **35**, 609 (1969).

[2] G. Küppers, Phys. Lett. **32A**, 7 (1970).

[3] R. M. Clever and F. H. Busse, J. Fluid Mech. **94**, 609 (1979).

[4] E. Bodenschatz, D. S. Cannell, J. R. de Bruyn, R. Ecke, Y. Hu, K. Lerman, and G. Ahlers, Physica D **61**, 77 (1992).

[5] Y. Hu, R. E. Ecke, and G. Ahlers, Phys. Rev. Lett. **74**, 5040 (1995).

[6] F. H. Busse and K. E. Heikes, Science **208**, 173 (1980).

[7] K. E. Heikes and F. H. Busse, Ann. N.Y. Acad. Sci. **357**, 28 (1980).

[8] K. Buhler and H. Oertel, J. Fluid Mech. **114**, 261 (1982).

[9] J. J. Niemela and R. J. Donnelly, Phys. Rev. Lett. **57**, 2524 (1986).

[10] F. Zhong, R. Ecke, and V. Steinberg, Physica D **51**, 596 (1991).

[11] F. Zhong and R. Ecke, Chaos **2**, 163 (1992).

[12] L. Ning and R. E. Ecke, Phys. Rev. E **47**, 2991 (1993).

[13] Y. Tu and M. Cross, Phys. Rev. Lett. **69**, 2515 (1992).

[14] M. Fantz, R. Friedrich, M. Bestehorn, and H. Haken, Physica D **61**, 147 (1992).

[15] M. Neufeld, R. Friedrich, and H. Haken, Z. Phys. B. **92**, 243 (1993).

[16] M. Cross, D. Meiron, and Y. Tu, Chaos **4**, 607 (1994).

[17] Y. Ponty, T. Passot, and P. Sulem, Phys. Rev. Lett. **00**, 00 (1997).

[18] A. Schluter, D. Lortz, and F. H. Busse, J. Fluid Mech. **23**, 129 (1965).

[19] S. Chandrasekhar, *Hydrodynamic and Hydromagnetic Stability* (Oxford University

importance of these processes at lower Ω suggests that they may also play a role for $\Omega \gtrsim 13$. This issue could be pursued theoretically by integrations of the Boussinesq equations with realistic boundary conditions. In addition, it may be possible to reduce these effects in an experiment (if they are present) by deliberately introducing an ϵ-variation from above to below threshold near the wall. This could be done for instance by a slight radial variation in the cell thickness.

Finally it is worth remarking that additional pattern-analysis techniques could be usefully employed in future studies of this system. These include variations on the Fourier methods described in this paper, as well as real-space analysis such as that used in some of our previous work[21,32]. Particularly useful may be the determination of the wave-director field in real space by fast computational methods advocated recently[35]. This should make it possible to develop algorithms for the direct determination of domain sizes and might avoid some of the ambiguities of correlation lengths determined by Fourier methods.

that it varied from about 59 to about 56° as ϵ varied from zero to 0.06. For comparison we calculated the growth rates of KL perturbations as a function of their angle Θ_{KL} and of ϵ. The experimental results for Θ_s differ from the calculated value $\Theta_{KL} = 43°$ for the angle at which the KL perturbations have their maximum growth rate at onset and for $\Omega = 15.4$. We conclude that the domain-front propagation selects an angle which is determined by nonlinear properties of the system and which is unrelated to the linear growth rate of the KL perturbations.

In the range $13 \lesssim \Omega \lesssim 20$ the pattern rotation-frequency in Fourier space is determined primarily by the domain switching. We made quantitative measurements of ω_a over this range of Ω and over a wide ϵ-range. We found that $\omega_a(\epsilon, \Omega)$ could be reduced to a single ϵ-dependent curve $\tilde{\omega}_a(\epsilon) \equiv \omega_a(\epsilon, \Omega)/\omega_r(\Omega)$. On the basis of Ginzburg-Landau models one would expect $\tilde{\omega}_a$ to be proportional to ϵ for small ϵ. We found that the data are difficult to reconcile with this prediction, and that a powerlaw with an exponent near 0.52 provides a good fit. When it is assumed that the leading ϵ-dependence is $\tilde{\omega}_a \propto \epsilon$, then large corrections of order ϵ^2 and ϵ^3 are required to fit the data over a significant range. We also determined a correlation length from the Fourier analysis of the data, and found similar problems in its interpretation. We have not yet been able to get reliable information about statistical properties like ω_a and ξ from the numerical integrations of the BE equations because much longer runs would be required for this purpose.

We close by pointing out some opportunities for additional work on this system. Perhaps the major remaining problem is that the origin of the anomalous ϵ-dependence of the switching frequency ω_a and of the correlation length remains largely obscure. Even though the anomalous behavior has been seen in two cells of quite different aspect ratio, it is difficult to rule out definitively that the dynamics is influenced by defects and fronts injected by the sidewall. Circumstantial evidence pointing in this direction is to be found in the larger domain size in the BE integration which used boundary conditions different from those relevant to the experiment. For the larger values of Ω, sidewall-induced processes are difficult to observe in the physical system because of the complexity of the patterns. The

V. SUMMARY AND CONCLUSIONS

We presented experimental results of patterns and their dynamics for Rayleigh-Bénard convection (RBC) in the presence of rotation about a vertical axis with an angular velocity Ω. For comparison with these data, we integrated the Boussinesq equations for RBC with rotation using some of the same parameter values as in the experiment. In this paper we focus on the range $8 \lesssim \Omega \lesssim 20$ where we observed patterns consisting of interacting domains of straight rolls. The domains exhibit a chaotic dynamics which consists primarily of domain-wall (or front) propagation by which a given domain tends to replace a neighboring one. The domain replacement (or switching) usually results in a re-orientation of the rolls in a given location through an angle $\Theta_s \simeq 58°$ in the direction of Ω. This "domain chaos" is typical of the parameter range where straight rolls are linearly unstable to Küppers-Lortz perturbations.

For $\Omega \lesssim 12$ the dynamics are difficult to interpret because they are strongly influenced by the nucleation of dislocation defects and fronts near the sidewalls. In this regime the dynamics is a mixture of sidewall-mediated front propagation and defect motion. We illustrate this parameter range with temporal pattern sequences, and we present quantitative measurements of the average pattern rotation-rate ω_a which results from the defect motion and front propagation.

With increasing Ω, and particularly close to onset, the dynamics became dominated by the nucleation of domain walls in the sample interior. Although a quantitative comparison has not yet been made, we found that the BE integrations yielded patterns with larger domains than the experiment. Although we do not know the reason for this difference, it is worth noting that the major difference between the experiment and the simulation is to be found in the boundary conditions at the sidewall.

In the intrinsic regime $13 \lesssim \Omega \lesssim 20$ where domain walls form spontaneously in the interior, the domain switching-angle Θ_s could be measured quantitatively for $\epsilon \lesssim 0.06$ by Fourier-transform analysis of the patterns. We found that Θ_s was independent of Ω and

to $\epsilon^{-1/2}$ would imply that this parameter should approach a constant value as ϵ vanishes. Unfortunately the data for $\epsilon < 0.04$ are not consistent with this expectation. A fit of

$$(1/\tilde{\xi})^2 = X_0\epsilon(1 + X_1\epsilon + X_2\epsilon^2) \tag{9}$$

to the data for $0.04 < \epsilon < 0.2$ is shown by the solid line in the figure. It gives the parameters $X_0 = 0.517$, $X_1 = -7.12$, and $X_2 = 20.4$. We note that X_1 and X_2 are similar in size to the corresponding coefficients $\omega_{a,1}$ and $\omega_{a,2}$ for the fit to $\tilde{\omega}_a$. For $\tilde{\xi}$, however, the deviation of the data for $\epsilon < 0.04$ is significant whereas for $\tilde{\omega}_a$ the fit was good for all $\epsilon < 0.2$. One might conjecture that the deviation for $\tilde{\xi}$ is caused by the finite size of the convection cell. Unfortunately, we have neither a theory nor sufficient data to test this hypothesis.

G. The Diffusivity D for $\Omega > \Omega_c$

In Ginzburg-Landau models, $D \equiv \xi^2\omega_a$ is independent of ϵ. In the previous section we saw that the correction terms in Eq. 6 for $\tilde{\omega}_a$ and in Eq. 9 for $1/\tilde{\xi}^2$ are of similar size. Thus they should nearly cancel in D, yielding a nearly ϵ-independent result. This is indeed the case. Using the unreduced data for ξ and ω_a, we obtained the diffusivities shown in Fig. 20. There is a sharp rise at small ϵ which is associated with the deviation of the data for $\tilde{\xi}$ from the fit of Eq. 9. Then there is an approximately constant region for $0.05 < \epsilon < 0.2$, and finally a decrease at higher ϵ. Averages of the data in the approximately constant range yield the solid lines in the figure. The average values are plotted in Fig. 21 as a function of Ω. Remarkably, the data show a simple Ω-dependence. They can be fit by the straight line $D = 0.53(\Omega - 10.5)$. Thus, although the individual dependences on ϵ of space- and time-scales do not follow the simplest predictions, the diffusivity is well behaved over a range of ϵ where KL front propagation is dominant over dislocation-defect nucleation and motion.

24

cients are $\omega_{a,0} = 3.34$, $\omega_{a,1} = -6.09$, and $\omega_{a,2} = 14.9$. We note that the coefficients of the higher-order terms are rather large, whereas *a priori* one might have expected them to be $\mathcal{O}(1)$. For comparison, the power-law fit (Eq. 5) is shown as a dash-dotted line. It is not as good a fit to the data, but it requires only two adjustable parameters. The dashed line in Fig. 16 is the leading term $\omega_{a,0}\epsilon$ of Eq. 6.

F. The Correlation Length ξ for $\Omega > \Omega_c$

Previously[5,21] we presented results for a correlation length $\xi(\epsilon, \Omega)$ which was defined[28] in terms of the second moment of $S(k)$. On the basis of GL models such a length would be expected to diverge as

$$\xi \propto \epsilon^{-1/2} \ . \tag{7}$$

This was found to be inconsistent with the data[5]. Instead a fit of the power-law

$$\xi = \xi_0 \epsilon^y (1 + D_\xi \epsilon) \tag{8}$$

to the data yielded $y \simeq 0.2$, in disagreement with the theory.

The successful collapse of the ω_a data suggests that a similar procedure might be applied to ξ. Here we use only the three data sets which were shown in Fig. 29 of Ref. [21] to avoid excessively crowded figures; but they adequately span the range $14 \leq \Omega \leq 20$ of the KL instability. We took the set at $\Omega = 14.3$ as the reference set, and divided the ξ-values of the other sets by an Ω-dependent reference value ξ_r to obtain $\tilde{\xi} \equiv \xi/\xi_r$. The resulting reduced correlation lengths are shown in Fig. 18, where the values of ξ_r are also given. One sees that the collapse is successful over a wide range of ϵ. A fit of Eq. 8 to $\tilde{\xi}$ for $\epsilon < 0.2$ yielded $\xi_0 = 4.64$, $y = 0.167$, and $D_\xi = -0.73$. This fit is shown as the dash-dotted line in the figure. It is excellent even beyond the fit range, *i.e.* for $\epsilon > 0.2$. But the value of y disagrees with the theory.

Encouraged by the successful fit of Eq. 6 to the data for $\tilde{\omega}_a$, we show in Fig. 19 the experimental results for $(1/\tilde{\xi})^2/\epsilon$ as a function of ϵ. An asymptotic proportionality of $\tilde{\xi}$

23

First we illustrate in Fig. 16 that the results for ω_a can be reduced, or collapsed, onto a single curve $\tilde{\omega}_a(\epsilon) \equiv \omega_a(\epsilon, \Omega)/\omega_r(\Omega)$ within their experimental uncertainties. We chose the data at $\Omega = 19.8$ as a reference set, and divided the results at the other values of Ω by an appropriately chosen Ω-dependent constant ω_r. Interestingly, the required ω_r (given in the figure caption) have a simple dependence upon Ω; within error they fall on a straight line given by

$$\omega_r = 0.129(\Omega - 12.16) . \tag{4}$$

The data collapse is successful for $\epsilon \leq 0.2$.

The reduced frequencies $\tilde{\omega}_a$ in Fig. 16 are shown on double-logarithmic scales. Thus a straight line in the figure corresponds to

$$\tilde{\omega}_a = \omega_{a,0}\epsilon^x . \tag{5}$$

The dashed line in the figure corresponds to $x = 1$, which would be consistent with Eq. 3. It clearly is a poor representation of the data. A fit of Eq. 5 to the data over the range $\epsilon < 0.2$ is represented by the dash-dotted line in the figure and gave $\omega_{a,0} = 0.575$ and $x = 0.518$. This result agrees with the previously-published analysis[5] which, however, was done for $\omega_a(\epsilon, \Omega)$ separately at each Ω. It fits the data quite well except perhaps at very small ϵ where the experimental uncertainties are largest. But the exponent $x \simeq 0.52 < 1$ is difficult to reconcile with the theory.

In an attempt to search further for an interpretation which retains the predicted $x = 1$, we show in Fig. 17 the ratio $\tilde{\omega}_a/\epsilon$ as a function of ϵ on linear scales. If Eq. 3 is valid, then the data should tend toward a constant value at $\epsilon = 0$. The data are indeed consistent with this expectation, but the large slope and the curvature suggested by the data indicate that a fit would require a function of the form

$$\tilde{\omega}_a = \omega_{a,0}\epsilon(1 + \omega_{a,1}\epsilon + \omega_{a,2}\epsilon^2) . \tag{6}$$

The solid line in the figure is a fit of this equation to the data. It clearly is an excellent representation, but it is a fit of a function with three parameters. The values of the coeffi-

of distinct domains was generally less than 3.

Measurements of ω_a for the , $= 23$ cell were limited to the region near onset. The results for $\Omega \leq 15$ are shown in Fig. 14. For a quantitative comparison, we fitted straight lines to $\omega_a(\epsilon, \Omega)$ for $\epsilon < 0.04$. As discussed before[5], this fitted the data quite well but, contrary to theoretical expectations, yielded finite values of ω_a at $\epsilon = 0$. In Fig. 15 we show the results for the slope $W = d\omega_a/d\epsilon$ for , $= 23$ (crosses) and , $= 40$ (solid circles). Both sets of data show a flat range of small W for $\Omega \lesssim 12$ and increasing W at higher Ω. Straight-line fits to $W(\Omega)$ in these two different regions gave an approximate Ω_0 at which the slope started to increase rapidly. For , $= 40$, Ω_0 was 12.5 ± 0.4 close to the theoretical Ω_c of 12.95 for $\sigma = 0.93$. For , $= 23$, Ω_0 was 12 ± 0.6 close to Ω_c for $\sigma = 0.83$. For Ω slightly above Ω_c the results for , $= 23$ are somewhat lower than those for , $= 40$. This may well be attributable to the fact that the dynamics at small ϵ had to be driven exclusively by bulk-nucleated KL fronts because of the absence of sidewall-nucleated fronts (see Sec. III B). At larger Ω the results for the two cells were more nearly equal.

E. Analysis of ω_a for , $= 40$ and $\Omega > \Omega_c$

We demonstrated previously[5] that it is difficult to reconcile the data for ω_a with the theoretical prediction

$$\omega_a \propto \epsilon \tag{3}$$

which is based on general properties of GL models and which is consistent with numerical integrations[16] of SH equations. For GL models one would expect Eq. 3 to be valid for sufficiently small ϵ. Here we review the interpretation of the experimental results, and then offer an alternative interpretation of the data which is consistent with Eq. 3, but which requires large analytic corrections to the linear variation. From a theoretical viewpoint the problem presented by the data can thus be reduced to the need to explain anomalously large coefficients of correction terms to the small-ϵ asymptotic behavior.

First we consider the range $\Omega \lesssim \Omega_c$ for $\Gamma = 40$. In Fig. 12 is a plot of ω_a versus ϵ for $8.8 \leq \Omega \leq 12.1$. At $\Omega = 10.5$, the dynamics at onset involved both KL-front and SV-defect motions, and ω_a increased with ϵ. As ϵ increased there was decreased activity of KL fronts relative to the SV defects, and ω_a decreased beyond $\epsilon \approx 0.1$, reflecting the difference between the contribution to ω_a of KL fronts and SV defects. Beyond $\epsilon \approx 0.2$, the dynamics was mostly mediated by the SV instability, resulting in smaller ω_a even though at higher ϵ the motion of SV defects became faster. This slowing down seemed to be caused by the accumulation of sidewall defects which interfered with KL-front nucleations. These sidewall defects began to nucleate traveling defects at higher ϵ, and at $\epsilon \approx 0.3$, KL activity was completely suppressed. Near $\epsilon \approx 0.5$ spirals appeared[21]. A similar dependence of ω_a on ϵ is seen in Fig. 12 for $\Omega > 10.5$ although the maximum value of ω_a was pushed to higher ϵ as Ω increased. This behavior may be attributable to similar pattern evolution, *i.e.* KL behavior being suppressed by dislocation-defect motion, as ϵ was increased.

D. The Domain-Switching Frequency ω_a for $\Omega > \Omega_c$

Next we examine the range $\Omega \gtrsim \Omega_c \simeq 13$ for $\Gamma = 40$. There the patterns were composed of many domains of differently oriented rolls, and the rapid changing of roll orientations was accomplished by moving fronts characteristic of the KL instability. Although SV defects may have been present in this parameter range, their presence was difficult to detect in the more complicated patterns. In any case, their much slower dynamics implies that their contribution to ω_a was minor or negligible. Nevertheless, the same trends of increasing ω_a near onset, reduced rate of increase at intermediate ϵ, and a gentle decrease for higher ϵ were seen throughout the range $10 \leq \Omega \leq 17$. This is evident in Fig. 13 which shows ω_a for $13 \leq \Omega \leq 20$. It is surprising that the behavior of ω_a remained quite consistent throughout the range $10 \leq \Omega \leq 17$ as the dynamics varied significantly at fixed ϵ as Ω changed. For $\Omega \gtrsim 13$ most fronts were nucleated away from the wall and often 5 or more domains were visible, whereas for $\Omega \lesssim 13$ KL fronts were generally initiated at the sidewall and the number

all very close to 58° with no systematic dependence on Ω and only a slight variation with ϵ. A fit to the data yielded the straight line. The average switching angle ranged only from about 59° near $\epsilon = 0$ to about 56° near $\epsilon = 0.06$. The lack of a discernible switching angle in the correlation function, when it occurs, is then a result of decoherence of the switching in different domains and of a broad distribution of Θ_s. Particularly for smaller Ω, the large variation in the switching angle from 40 to 70 ° and the additional angular change arising from defect motions prevents the determination of $< \Theta_s >$.

For $\Omega > \Omega_c$ it is interesting to ask what relationship (if any) $< \Theta_s >$ may have to the angles Θ_{KL} of the infinitesimal KL perturbations with positive growth rates $s(\Theta_{KL})$. For $\Omega > \Omega_c$ there is a continuous band of such angles, and s has a positive maximum at a particular angle which is usually associated with the KL instability. In Fig. 11 we show $s(\Theta_{KL})$ as a function of Θ_{KL} for $\Omega = 15.4$ and $\sigma = 0.93$ as an example. Here s was evaluated for the average pattern wave-number $k = k_c - 1.45\epsilon$ found[21] in the experiment. The wave number of the KL perturbation was chosen so as to maximize $s(\Theta_{KL})$. The range of $< \Theta_s >$ chosen by the experiment as ϵ varied from zero to 0.06 (solid line in Fig. 10) is shown by the short horizontal bar from 56 to 59°. We see that $< \Theta_s >$ is at the extreme upper end of the range where $s(\Theta_{KL}) \simeq 0$. This suggests that there is in fact no relationship between Θ_{KL} and Θ_s, and that Θ_s is chosen by nonlinear selection processes inherent primarily in domain-front propagation which are not understood in detail and which are unrelated to the linear instability.

C. The Pattern-Rotation and Domain-Switching Frequency ω_a at small Ω

We now consider the characteristic switching frequency. Since Θ_s was found to be essentially constant for $\Omega \gtrsim 13$, the average rotation rate in Fourier space ω_a is, to a good approximation, proportional to the discrete inverse switching time τ_d when domains are present. When there are no domains, ω_a is much smaller and represents pattern rotation dominated by dislocations and other defects[21].

was fairly constant for most of the sequence.

The two-dimensional auto-correlation function $C(\delta\Theta, \delta t)$ of $F(\Theta, t)$ (see Sec. II B) enhances the angle-time plots in a manner that emphasizes the average domain switching. In Fig. 9 we show $C(\delta\Theta, \delta t)$ corresponding to Fig. 8. No discrete switching is seen in Fig. 9b because no domains were present in real space. The other examples show differing degrees of short-time correlations corresponding to the domain switching. It is possible to measure both the average switching angle $< \Theta_s >$ and the switching frequency ω_a as functions of ϵ and Ω over a significant parameter range. However, the existence of multiple domains and the mixing of the effects of KL fronts and defects generated by the skewed-varicose instability (SV defects)[21] prevented the measurement of $< \Theta_s >$ over some other parameter ranges. In practice, the angle could only be determined for $\epsilon \leq 0.06$ and $\Omega \geq 12$, and then only for some image sequences. This is a shortcoming of the analysis method as visually the domains still switched discretely even when the angle-time plot was unable to pick up these changes. This difficulty precluded directly measuring the switching time τ_d for those sequences where $< \Theta_s >$ could not be determined. Thus we report instead the angular change ω_a per unit time which can be measured from either the angle-time plots, *e.g.* Figs. 8, or from the auto-correlation plots, *e.g.* Figs. 9. This could introduce a systematic difference between the actual switching time and our measured angular rate of change if the switching angle varied appreciably with ϵ and Ω. With that in mind we consider first the measurement of $< \Theta_s >$.

B. The Domain Switching Angle $< \Theta_s >$ for $, = 40$

The angle-time plots in Figs. 2a and 8d are good examples of sequences for which an accurate value of $< \Theta_s >$ could be easily obtained. In the auto-correlations, Figs. 2b and 9d, the constant angular change per KL switching is apparent as the distance between the relatively evenly-spaced bright spots. The switching angles are plotted against ϵ in Fig. 10 for the values of Ω and ϵ where the technique was sufficient to extract them. The angles were

IV. QUANTITATIVE IMAGE ANALYSIS

A. Angle-Time Plots and their Correlation Functions for $\varsigma = 40$

Figure 8a shows the angle-time plot of $F(\Theta, t)$ (see Sec. II B) for $\Omega = 8.8$ and $\epsilon = 0.04$. It corresponds to the same run as the image sequence in Fig. 5, but is composed of the complete 257 images of the run. The total duration of this run was $9600\tau_v$. Most of the time the cell contained primarily one domain, so there was a dominant roll orientation. This led to the bright irregular clusters, some of which we identified by plusses in the upper part of the figure. The clusters trace out a temporal sequence representing the time evolution of the roll orientation. Lines drawn through them have a small positive slope equal to a characteristic inverse frequency ω_a^{-1}. For this example the switching angle Θ_s varied from less than $40°$ to close to $90°$. This wide distribution is characteristic of the range of $\Omega < \Omega_c$ where the domains are primarily wall-nucleated.

At the same Ω and higher ϵ KL fronts became less frequent, and defect motion dominated the dynamics. The angle-time plot of a $4800 \ \tau_v$ sequence for $\epsilon = 0.16$ is shown in Fig. 8b. No KL fronts were observed in these images. The dominant roll orientation changed smoothly at a constant rate. The change was caused by defect nucleation and propagation and was rather slow compared to the KL switching process shown in the other angle-time plots.

As Ω was increased, the average size of the KL domains became smaller, and a single domain rarely dominated the pattern. At $\Omega \gtrsim 11$, there was always more than one domain in the cell. A typical angle-time plot at $\Omega = 12.1$ and $\epsilon = 0.11$ is shown in Fig. 8c. This run contained the image sequence shown in Fig. 6. Even though more than one domain was present, there was usually a dominant orientation in the cell center (in the analysis the center is emphasized by the use of the Hanning window). A dominant orientation remained discernable from the angle-time plots even at higher ϵ and/or Ω. An example, at $\Omega = 16.5$, is shown in Fig. 8d which was produced from the complete image sequence corresponding to Fig. 7. The light spots are arranged in regular intervals as the domain switching angle

as shown in the time sequence in Fig. 6. In addition to fronts nucleated at the sidewall, occasionally new fronts appeared spontaneously in the interior of the cell. With increasing ϵ the spontaneous front nucleation away from the wall became more frequent. One such front is indicated by the arrow in Fig. 6d.

At higher Ω, front motion continued to dominate the dynamics, although defects still played a role. The rolls tended to terminate with their axes more nearly perpendicular to the sidewall[21], as seen in Fig. 7. It is possible that this tendency influenced the dynamics. Defect nucleation in an otherwise uniform domain was sometimes observed as well, as shown in Fig. 7g which contains a pair of such defects.

the sidewall was still in the conduction state[21]. Consequently, for $\epsilon \lesssim 0.02$, there were no sidewall-nucleated domains and thus no KL dynamics. Thus the behavior of the , $= 23$ cell supports the idea that the KL dynamics for the , $= 40$ cell at onset and below Ω_c is sidewall-mediated.

C. Dynamics for , $= 40$

We now return to the , $= 40$ cell and illustrate the KL dynamics in temporal sequences of images. By $\Omega = 8.8$, KL domains and fronts occurred at the onset of convection and were responsible for much of the dynamics, as seen in the time sequence of Fig. 5. Here the images are for $\epsilon = 0.04$ and were taken at time intervals of 80 τ_v. The fronts were nucleated at the wall. Figure 5c illustrates a case where two fronts merge in the cell interior. The region enclosed by the circle in Fig. 5d gave rise to the domain circled in Fig. 5e. From time to time the cell was almost completely occupied by a single domain, as in Fig. 5g. Such occurrences were never observed for $\Omega \gtrsim 12$. Much defect movement occurred along the advancing front between the stable and unstable rolls. This is illustrated by the well-defined front in the upper right of Fig. 5f. The rolls behind this growing front joined with the unstable rolls in Fig. 5g, and the defects that seperated the two sets of rolls propagated toward the right, leaving behind joined rolls with kinks which gradually smoothed out. Even with this smoothing process, the overall roll orientation still changed by discrete steps, but the changes varied from 30 to 90 degrees. This is qualitatively different from the smooth angular changes induced by repeated dislocation-defect motion which dominated the dynamics for $5 \lesssim \Omega \lesssim 10$ at higher ϵ[21]. There the orientation of the underlying roll pattern advanced slowly in the direction of rotation. Although occasional KL fronts were initiated either by the sidewall or by the clusters of defects next to the sidewall, these fronts only affected a small portion of the cell and rarely propagated across the whole cell.

At $\Omega = 12.7$ the KL fronts which originated near the sidewall remained dominant in the dynamics, but the pattern always contained several domains with different roll orientations

15

as illustrated in Fig. 4. For $\Omega \lesssim 10$, KL fronts became less frequent. The patterns became S-shaped, and two large sidewall foci usually appeared as shown in Fig. 4a. On the side clockwise from the foci, rolls ended with their axes nearly perpendicular to the sidewall whereas on the other side rolls terminated more obliquely. This is in contrast to the sidewall foci seen for $\Omega = 0$[32] which were highly symmetric. Dislocation defects appeared from the side of the foci with rolls perpendicular to the wall and travelled across the cell, disappearing on the opposite side. The direction of defect motion is determined by their topological charge and the direction of cell rotation[21]. Compared to lower ϵ, the rate of nucleation of defects was higher, but no sidewall accumulation of defects was observed. As for lower ϵ, KL domains and fronts began to dominate as Ω increased, as seen in Fig. 4b-d. Again we found that the domain size in the BE integration was larger than in the experiment at a given Ω. Cellular regions seemed less abundant than in the experiment, as was found at smaller ϵ.

Although we do not yet have a quantitative comparison, it is apparent from Figs. 3 and 4 that the domains in the BE integration are generally larger than those in the experiment. We do not know the reason for this difference, but note that the major difference between experiment and simulation is to be found in the boundary conditions. Simulations with realistic sidewall boundary conditions would thus be very desirable, but have not yet been performed.

B. Patterns for $\Gamma = 23$

Except for their size, the patterns encountered in the smaller $\Gamma = 23$ cell were generally similar to those of the $\Gamma = 40$ cell. A few examples were presented in Ref. [21], and we will not discuss them any further. The major difference between the two existed close to onset and for $\Omega < 12$, where the small cell showed a bifurcation to a time-independent state without any KL domains (see Fig. 16 of Ref. [21]). We believe that this is the result of the small radial variation of the cell thickness mentioned above which caused a rounded transition to convection, with rolls appearing first in the central region while the region near

$\Omega \geq 8.8$, representative patterns from the experiment and corresponding images from BE integrations are shown in Figs. 3 and 4 for $\epsilon = 0.06$ and $\epsilon \approx 0.17$ respectively.

We first consider the small-ϵ range represented in Fig. 3. For $8 \lesssim \Omega \lesssim 11$, the patterns at onset were time dependent, with KL domains and fronts initiated by crossrolls at the sidewall. The domains grew into the unstable central region of the cell. A typical front generated in this manner is visible near the center of the cell in Fig. 3a. The phenomena are similar to previous observations[10] for , $= 10$ and $\sigma = 6.4$. Dislocation defects were also abundant and active in the same parameter range; some of them can be seen in the upper-left quarter of Fig. 3a. Qualitatively the same phenomena were found also in the GL[13] and SH simulations[14,15], as well as in our BE integrations (Fig. 3e).

For $\Omega = 12.7$ (Fig. 3b), a typical pattern looked very similar to those at $\Omega = 8.8$, but the dynamics showed an important difference: although most KL fronts were still initiated at the sidewall, some fronts appeared spontaneously in regions away from the sidewall. The smallest Ω at which nucleation of fronts in the cell interior was observed was 10.5. Cellular regions where two sets of differently-oriented rolls co-existed began to appear, as seen in Fig. 3b. The cellular regions were not fixed in space. As the domains evolved in both size and shape via KL fronts, different regions appeared cellular at different times. The BE integration yielded similar patterns, as shown in Fig. 3f, although cellular regions seemed to be somewhat less abundant.

At $\Omega = 16.5$, Fig. 3c, the average size of a domain was much smaller than for $\Omega \lesssim 12$ and cellular regions were more abundant. Here a noticeable difference between the experiment and the BE integration becomes apparent. In the numerically generated image (Fig. 3g) the domains are significantly larger than in the experiment, and cellular regions are less abundant. The trend in the experiment with increasing Ω of decreasing domain size and increasing occurence of cellular regions persisted up to the highest $\Omega \simeq 20$ investigated, Fig. 3d. Although the BE integrations showed similar trends, the changes with Ω were less pronounced.

As ϵ was increased to about 0.17, there were some changes in the nature of the patterns

for obtaining semiquantitative results. With respect to the horizontal directions a Fourier expansion was used. By projecting on the linear eigenmodes the linear parts of Eqs. 1 and 2 are diagonalized; in the simulations usually three " active " modes are kept (see Ref. [34]).

Within our approach, where a periodic regime is assumed, it is strictly speaking impossible to incorporate lateral boundary conditions as required in a circular cell. To deal approximately with this situation we put all fields to zero at each timestep outside the cell radius. One recovers in simulations some features at the boundaries (*e.g.* small cross roll patches) familiar from experiments. On the other hand, the tendency of rolls to terminate with their axes perpendicular to the boundary is less pronounced.

All simulations in this paper are made on a 256×256 horizontal grid for $\sigma = 1$, with the same aspect ratio , $= 40$ as in the experiments. Representative results from experiments and simulations at the same parameter values are presented in Figs. 3 and 4.

III. QUALITATIVE DESCRIPTION OF PATTERNS AND THEIR DYNAMICS

Here we give a qualitative description of the patterns and their dynamics in the parameter regimes where the KL instability was the dominant mechanism for time dependence. The patterns and dynamics at smaller Ω and larger ϵ were presented earlier[21]. Except for small Ω and ϵ, the patterns in the , $= 40$ and , $= 23$ cell were very similar and only the former is described in detail. Recall that the , $= 23$ cell had a small radial variation in height which had interesting effects near onset for $\Omega < \Omega_c$ which we describe briefly below in Sec. III B (see also Ref. [21]).

A. Patterns for , $= 40$

For , $= 40$, no Küppers-Lortz domains were observed for $\Omega \lesssim 5$ up to $\epsilon \approx 1$ where spiral-defect chaos dominated. The first appearance of KL domains was at $\Omega = 6.6$ and $\epsilon = 0.08$ although there the main time dependence was still due to dislocation motion. For

are well-defined domains which form a temporal succession. Alternatively, one sees that the temporal succession of the bright clusters in Fig. 2 defines a set of lines with a small positive slope. We have drawn one such line (dashed) in Fig. 2b to guide the eye. Its slope likewise characterizes the time scale of the KL dynamics, and we use its inverse ω_a as the characteristic frequency. This has the advantage that ω_a can be determined even for relatively small Ω where domain switching is absent and where τ_d thus is not defined. In that parameter range ω_a represents an overall pattern rotation mediated primarily by dislocation defects[21]. Presumably small contributions from defect nucleation and possibly other processes which are difficult to identify in complicated patterns also contribute to ω_a in the KL parameter range; but domain switching seems to dominate there since it is faster and more abundant.

C. Numerical Integrations

The nondimensionalized Boussinesq equations (BE) for RBC with rotation read as follows (see e.g. Ref. [3]):

$$\sigma^{-1} \left(\frac{\partial \mathbf{u}}{\partial t} + \mathbf{u} \cdot \nabla \mathbf{u} \right) = -\nabla \pi + \nabla^2 \mathbf{u} + \hat{\mathbf{e}} \Theta + \Omega \hat{\mathbf{e}} \times \mathbf{u} \tag{1}$$

$$\frac{\partial \Theta}{\partial t} + \mathbf{u} \cdot \nabla \Theta = \nabla^2 \Theta + R \hat{\mathbf{e}} \cdot \mathbf{u} \tag{2}$$

where $\hat{\mathbf{e}}$ is the unit vector in the z direction. The velocity field $\mathbf{u}$ and the deviation Θ of the temperature from the diffusive linear profile vanish at the horizontal boundaries of the cell. Incompressibility ($\nabla \cdot \mathbf{u} = 0$) is assumed, which allows the introduction of poloidal and toroidal velocity potentials [3] instead of the three velocity components. Moreover, the pressure π can be eliminated. Numerical simulations of Eqs. 1 and 2 were performed by the use of the techniques already described elsewhere in some detail [33,34]. With respect to the vertical coordinate z, all fields are expanded in a set of appropriate functions that vanish at the boundaries (Galerkin method). We found that even two such functions were sufficient

11

at numerous wave vectors as seen in Fig. 1c; but even then two or three orientations often dominate the part of the sample emphasized by the window function. The major drawback of this analysis is the loss of local spatial information. For instance, this method cannot distinguish rolls with the same wave vector in several disconnected domains from rolls in a single larger domain. Nonetheless, it has yielded abundant information on the evolution of the "average" roll orientation of the patterns.

Examples of the computation of $S(k)$ and its various moments have been given elsewhere[28]. Here we illustrate the use of angle-time plots of $F(\Theta, t)$ and of the corresponding $C(\delta\Theta, \delta t)$. Figure 2a shows $F(\Theta, t)$ for $\Omega = 15.4$ and $\epsilon = 0.027$. The horizontal axis spans $0 < \Theta < \pi$, and the vertical axis covers a time interval of 2080 τ_v, with time increasing in the upward direction. Figure 2b is the corresponding $C(\delta\Theta, \delta t)$. Here the origin is in the center, the horizontal axis spans $-\pi/2 < \delta\Theta < \pi/2$, and the vertical axis runs from $-1040 < \delta t < 1040 t_v$. As expected, $C(\delta\Theta, \delta t)$ has all the same features as $F(\Theta, t)$, except that they are smoothed by the averaging involved in computing it. A noticeable feature of $F(\Theta, t)$ is the temporal succession of bright clusters corresponding to large values. Each cluster corresponds to a time when a domain with a particular roll orientation dominated the central portion of the sample which is emphasized by the Hanning window. The angular change Θ_s between successive clusters yields the difference in domain orientation between temporally successive domains. In $C(\delta\Theta, \delta t)$ this angular distance is an average $< \Theta_s >$ over the distribution of such angular changes. Sometimes Θ_s is apparent even in single snapshots of $F(\mathbf{k}, t)$ such as the one in Fig. 1c. This happens when two domains contribute significantly near the center of the cell. Depending on the ϵ and Ω range, we found that Θ_s could be very well defined or could have a broad distribution. When it had a narrow distribution, then the bright clusters in $F(\Theta, t)$ tended to fall on lines which in Fig. 2 run from the top left to the bottom right. In Fig. 2b we have drawn three such lines to guide the eye.

The time interval between two temporally successive bright clusters defines a lifetime of a KL domain, or a domain-switching time τ_d. τ_d is defined, however, only when there

For the work discussed in the present paper, approximately 130,000 images were analyzed.

B. Image Analysis

We used the time evolution of the modulus $F(\mathbf{k}, t)$ of the spatial Fourier transform and of the structure factor $S(\mathbf{k}, t)$ [the square of $F(\mathbf{k}, t)$, also known as the spatial power spectrum] to determine the spatial and temporal structure of KL-unstable states. Often it was useful to average $S(\mathbf{k}, t)$ over time to give $S(\mathbf{k})$. Although there may be some ambiguities of interpretation because of the combination of influences that determine the shape of $S(\mathbf{k})$[31], this method allows the rapid, efficient analysis of many images and is unambiguous in its definition. We used the angular distribution $F(\Theta, t)$, $0 < \Theta < \pi$, obtained by averaging $S(\mathbf{k}, t)$ over $|\mathbf{k}|$ in the upper half-plane $k_y > 0$ [$\mathbf{k} = (k_x, k_y)$], and made angle-time plots of $F(\Theta, t)$[10,11]. The auto-correlation function $C(\delta\Theta, \delta t)$ of $F(\Theta, t)$ yielded averaged information about the dynamics[12]. Alternatively, we averaged $S(\mathbf{k})$ over Θ to obtain $S(k)$. The first moment of $S(k)$ yielded a mean wave-number $\bar{k}$, and its second moment about $\bar{k}$ gave the inverse square ξ^{-2} of a length scale ξ[28]. We now illustrate these analysis methods with examples.

For grey-scaled graphical representations of the Fourier transform we found $F(\mathbf{k}, t)$ to be preferable to $S(\mathbf{k}, t)$ because a smaller grey-scale resolution was sufficient to convey the nature of the structure in $\mathbf{k}$-space. In Fig. 1 we show three examples of images and the corresponding $F(\mathbf{k}, t)$. The Fourier transforms were done after multiplying the image by a Hanning window as described elsewhere[32]. Thus the rolls near the center of the image contributed primarily to $F(\mathbf{k}, t)$, and the rolls near the sidewall were de-emphasized. The single-domain nearly-straight rolls in Fig. 1a yield contributions only at a nearly-unique angle corresponding to the direction of the dominant $\mathbf{k}$. For patterns containing multiple domains of different roll orientations or curved rolls near the cell center, as in Fig. 1b, $F(\mathbf{k}, t)$ contains two or more pairs of arcs of greater angular extent. In the fully-developed KL state, where many domains are present simultaneously in the cell, there are contributions

II. APPARATUS, IMAGE ANALYSIS, AND INTEGRATION OF THE BOUSSINESQ EQUATIONS

A. Apparatus

The apparatus is described thoroughly elsewhere[21,29,30]. Most of the data presented here were obtained from a circular convection cell with a diameter of 86 mm and a height of 1.06 ± 0.002 mm ($, = 40$). The cell was filled with CO_2 at 33.1 bar. This pressure was held constant within 0.005%. The temperature of the bath which cooled the top plate was held constant within ± 0.0002°C near 33.7 °C. Under these conditions, the fluid had a Prandtl number of 0.93. The vertical thermal diffusion time $\tau_v = d^2/\kappa$ was 4.5 sec, and the horizontal thermal diffusion time $\tau_h = ,\,^2\tau_v$ was 7200 sec. The measured $\Delta T_c(\Omega = 0)$ was 1.487 ± 0.004 °C, in good agreement with the value 1.47 °C calculated from the fluid properties and the cell thickness.

We also made measurements in a $, = 23$ cell with $d = 0.201$ cm and CO_2 gas pressure of 16.6 bar. In this cell, a thinner sapphire window (3.2 mm) was used for the cell top, and the small pressure differential between the gas sample and the water bath caused a slight bowing of the cell in the middle, but left the cell profile approximately axisymmetric. Due to the maximum height at the center[21], a convection pattern first appeared there at $\epsilon = -0.015$ and filled the cell for $\epsilon \geq 0.012$. For this cell, τ_v was 6.7 sec and σ was 0.83.

Each cell was placed inside a pressure vessel mounted on a turntable driven by a stepper motor through a belt-and-pulley arrangement with one revolution of 360° completed in 50,000 microsteps. For the $, = 40$ cell, 1 Hz was equivalent to $\Omega = 30$. The effect of the centrifugal force at the highest rotation rate in the experiments of 0.7 Hz was small, with $(2\pi f)^2 \cdot , d/g = 0.09$. The rotation direction was counterclockwise as viewed from above. The convection patterns were observed by the shadowgraph-visualization method[30] in the rotating frame. The contrast-enhanced images in this paper show black regions corresponding to hot fluid (upflow) and white regions corresponding to cold fluid (downflow).

by GL equations if they involve rapid spatial variations. On the other hand, the difference between theory and experiment may possibly be found in the influence of the experimental cell sidewall, which seems to have a much larger influence for a rotating system than for a stationary one[21]. In particular, measurements for $\Omega < \Omega_c$ have shown that defects and KL domain walls tend to be injected into the sample interior in the rotating system. Although (as described below) we have seen no aspect-ratio dependence of the KL dynamics above Ω_c and no evidence for the importance of wall-nucleated defects or domain walls in the KL state above Ω_c, it is difficult to rule out completely that the cell walls play a role, except perhaps by comparison with numerical integrations of the Boussinesq equations with realistic sidewall boundary conditions. Such calculations have not yet been done.

In this paper, we present a detailed description of patterns and their dynamics in the KL-unstable regime. A comparison is made between experimental patterns and patterns generated by integration of the Boussinesq equations. We then concentrate on the time scale of the dynamics and its dependence on system size and boundary conditions, and present experimental results for a domain switching-angle Θ_s and theoretical results for the angle Θ_{KL} of the KL perturbation with the maximum growth rate at onset. Characterization of the pattern wave-number and the spatial correlation length over the entire range of Ω encompassing the KL region were reported previously[21] but are re-examined here.

In Sec. II we briefly describe the experimental apparatus, the image-analysis procedures, and the integration of the Boussinesq equations. The overall pattern dynamics are discussed in Sec. III. Quantitative analysis of the time and length scaling and results for Θ_s are presented in Sec. IV. Conclusions and future prospects are discussed in Sec. V.

Perhaps most relevant to the present experiment are the simulations and pattern analysis based on a SH model by Cross *et al.*[16]. As is done for experimental images[28], they computed the structure factor $S(\mathbf{k})$ (the square of the modulus of the Fourier transform) corresponding to their numerical integrations of the SH model. From it they obtained a correlation length equal to the inverse of the half-width of $S(k)$. They concluded that the main features of the KL dynamics are not substantially altered from that predicted using the more restrictive 3-mode GL model[13]. They also found for the SH model that the correlation length was approximately proportional to $\epsilon^{-1/2}$. The data were not sufficient to determine the dependence of ω_a on ϵ.

The above summary shows that there are a number of properties of the system which are found both in experiment and theory. At the linear level there is quantitative agreement about $R_c(\Omega)$ and the critical wavenumber $k_c(\Omega)$[21]. At the weakly-nonlinear level both theory and experiment yield a supercritical bifurcation. The main characteristic of the KL state common to experiments and models is the existence of domains, with one domain invading another by domain-wall motion. This feature suggests the name "domain chaos" for the KL state. The existence of KL domains below Ω_c can be understood in terms of domain walls emanating from the sidewall of the finite experimental system and is consistent with a finite domain-wall speed found in the models below Ω_c.

There remain two major issues on which theory and experiment yield different answers. These are the typical length and time scales which describe the KL state. The experiment finds that they are approximately proportional to $\epsilon^{-0.2}$ and $\epsilon^{-0.5}$ respectively at small ϵ, whereas the theoretical models yield $\epsilon^{-1/2}$ and ϵ^{-1} in the limit as ϵ vanishes. If one tries to interpret the experiment by retaining the leading theoretical exponents, large corrections to the asymptotic behavior at small ϵ are required which do not seem to have a basis in the theoretical models. The theoretical leading exponents are inherent in the structure of GL equations, and it is not obvious how to change them. As one possible source of the discrepancy between theory and experiment, we note that the dynamics of the KL state is dominated by fronts. They are associated with lines of defects which may not be describable

6

a range of Ω and σ, and that it approaches[22] 59.7° for large σ and $\Omega > \Omega_c \simeq 27.4$. This led to the use by Busse and Heikes[6] of a three-mode model[23] with $\Theta_s = \Theta_{KL} = 60°$. The model consisted of three coupled amplitude equations, one for each of three roll orientations. Since it did not include spatial variation, it is not suitable for the description of the intricate patterns consisting of domains which were seen in the experiments[4–7,10,11]. In order to produce persistent chaotic dynamics, a noise term (presumably representing the influence of other modes which the model neglects) had to be added. More recently [13] certain spatial-derivative terms have been added to this model, thus obtaining three coupled Ginzburg-Landau (GL) equations. This model yielded persistent chaotic dynamics without the addition of noise and produced domains of different roll orientations in different spatial locations. The time dependence consisted primarily of domain-wall motion, as seen in the experiments. The model also offered an explanation for the experimentally observed[10,4,11] KL-like state below Ω_c: the domain-wall speed is non-zero below Ω_c, so if an interface exists, it can propagate and cause roll-switching even for $\Omega < \Omega_c$. In the experiments the patterns contained grain boundaries or defects near the sidewall, and fronts could be nucleated by these structures.

Despite their successes, the 3-mode models just described can not capture effects associated with departures of Θ_s from 60 °, with the distortions of rolls such as roll curvature and wavenumber variations, and with the influence of large-scale circulation important for small σ. To investigate the qualitative influence of these factors, the Swift-Hohenberg (SH) equation[24] was extended to include terms associated with rotation[14–16]. This provided a reasonable model for high-Prandtl-number fluids. Numerical studies based on it[14,15] have qualitatively reproduced experimental observations of sidewall-initiated front-propagation caused by the KL instability. In addition to the KL dynamics, these simulations yielded rigid pattern rotation, gliding defects, and defect-induced rotation at moderate Ω and ϵ[25–27]. These latter phenomena have been studied in recent experiments[21]. More recently, mean flow[17] has been coupled to the SH equation, thus providing a model for finite-Prandtl-number effects.

Ω less than the theoretically expected Ω_c. The angle Θ_s between domains was found to be generally greater than the predicted KL angle of about 60° [20]. Later experiments by others[10], also using water and a cell with a radius-to-height ratio , = 15, recorded patterns down to $\epsilon \approx 0.1$ and also found KL domains well below the predicted Ω_c. The measured Θ_s, however, agreed well with theoretical predictions for Θ_{KL}. For smaller σ, experiments using liquid ^4He and a cell with , $\simeq 10$ showed that the heat transport became time dependent at the onset of convection for $\Omega \approx 9$, fairly close to $\Omega_c \simeq 10$ at their Prandtl number of 0.7[9]. There was, however, no flow visualization and thus no spatial information was obtained. No experiments had provided the combination of large , , small ϵ, and flow visualization necessary for a quantitative study of the KL instability near onset.

Other issues addressed by the experiments were the length- and time-scales ξ and ω_a^{-1} which characterize the KL-unstable patterns and their dynamics. Heikes and Busse[6,7,20] found $\omega_a^{-1} \propto \epsilon^{-3/4}$ for their ϵ-range well above the convective onset. In the liquid-helium experiments[9] a broad-band non-periodic time dependence was observed in the heat transport near onset which yielded a characteristic frequency proportional to $\epsilon^{1/2}$; but without flow visualization the interpretation of this global measurement for a relatively small cell in terms of the KL state is uncertain because of other possible sources of time dependence. Our previous measurements based on the patterns at small ϵ showed[5,21] that the time scale is approximately proportional to $\epsilon^{-0.5}$, consistent with the helium experiments. They also gave a length scale approximately proportional to $\epsilon^{-0.2}$. As we will see below, these results are difficult to reconcile with various model equations which generally yield $\omega_a \propto \epsilon^1$ and $\xi \propto \epsilon^{-1/2}$.

The theoretical work of Küppers and Lortz [1,2] demonstrated that straight rolls are unstable at the onset of convection when $\Omega > \Omega_c$, but the theory made no predictions about the spatial patterns produced by the instability. Non-linear stability analysis by Clever and Busse[3] provided additional details about the instability, including the dependence of Θ_{KL} on Ω and σ. There was, however, relatively little information for σ near one, which is of interest in the present work. It is known that Θ_{KL} varies between 10° and 60° over

4

I. INTRODUCTION

The Küppers-Lortz (KL) instability occurs in Rayleigh-Bénard convection (RBC) with rotation about a vertical axis[1,2]. It is of interest for several reasons. One of these is that one expects a *supercritical* bifurcation from the spatially-uniform conduction state directly to a KL-unstable state of convection[3]. The instability produces spatio-temporal chaos (STC) immediately above onset[4,5]. Thus the KL instability offers a rare opportunity to study STC in a parameter range where weakly-nonlinear theories should be applicable. After receiving only limited attention for several decades[1–3,6–9], there has been renewed interest in it both among experimentalists[4,5,10–12] and theorists[13–17].

Without rotation, straight, parallel rolls are predicted just beyond the onset of RBC when the temperature difference ΔT across the fluid layer exceeds a critical value ΔT_c[18]. The dimensionless control parameter for this system is the Rayleigh number $R = g\alpha d^3 \Delta T/\nu\kappa$ where g is the acceleration of gravity, α is the thermal expansion coefficient, d is the layer depth, ν is the kinematic viscosity, and κ is the thermal diffusivity of the fluid. The critical value $R_c = R(\Delta T_c)$ is equal to 1708[19]. With rotation, there is an additional control parameter, namely the dimensionless rotation rate $\Omega \equiv 2\pi f d^2/\nu$ where f is the rotation rate in Hz. As a function of Ω, $\Delta T_c(\Omega)$ (and thus $R_c(\Omega)$) increases[19]. The critical Rayleigh number $R_c(\Omega)$ is independent of the Prandtl number $\sigma \equiv \nu/\kappa$. For $\Omega > \Omega_c(\sigma)$, the KL instability is predicted[1–3] to occur at $R_c(\Omega)$. It is an instability of a set of parallel straight rolls of a given orientation to a short-wavelength perturbation at an angle Θ_{KL} relative to these rolls. The angle Θ_{KL} is advanced in the direction of Ω.

The seminal experiments of Heikes and Busse[6,7] using water and shadowgraph flow-visualization were for $\epsilon \equiv \Delta T/\Delta T_c - 1 \gtrsim 0.5$ and for large aspect ratios. They confirmed the existence of the KL-unstable state and showed that the patterns resulting from the instability consisted of domains of rolls, characterized by a more or less uniform roll orientation within a given domain. As a function of time, a replacement of one set of unstable rolls by another occurred via domain-wall (front) propagation. At large ϵ, the instability was observed for

the systems were qualitatively similar. For $\Omega \gtrsim 12$ there was no qualitative difference in the bahavior of the two cells at any ϵ. The average size of a domain containing rolls of approximately the same orientation decreased with increasing Ω, and the time dependence speeded up and became dominated by domain-wall propagation. The numerical solutions were qualitatively similar, although there was a tendency for the domains to be larger at the same ϵ and Ω. The replacement of domains of one orientation by those with another led to a rotation in Fourier space which was characterized by a rotation frequency ω_a in the frame rotating at angular velocity Ω. Quantitative experimental measurements of ω_a, of a correlation length ξ, and of a domain-switching angle Θ_s as functions of $\epsilon \equiv \Delta T/\Delta T_c - 1$ and Ω are presented. For $13 \lesssim \Omega \lesssim 18$, Θ_s was independent of Ω and close to $58°$. We computed the angle of maximum growth rate Θ_{KL} of KL perturbations, and found it to be $43°$, distinctly different from Θ_s. The results for $\omega_a(\epsilon, \Omega)$ over the range $13 \lesssim \Omega \lesssim 20$ can be collapsed onto a single curve $\tilde{\omega}_a(\epsilon) \equiv \omega_a(\epsilon, \Omega)/\omega_r(\Omega)$ by applying an Ω-dependent factor $1/\omega_r$. Similar collapse can be accomplished for $\tilde{\xi}(\epsilon) = \xi(\epsilon, \Omega)/\xi_r(\Omega)$. An analysis of $\tilde{\omega}_a(\epsilon)$ and $\tilde{\xi}(\epsilon)$ in terms of various functional forms is presented. It is difficult to reconcile the ϵ-dependence of $\tilde{\omega}_a$ and $\tilde{\xi}$ at small ϵ with the theoretically expected proportionality to ϵ and $\epsilon^{-1/2}$ respectively.

Convection Under Rotation for Prandtl Numbers Near One: Küppers-Lortz Instability

Yuchou Hu[1,2], Werner Pesch[3], Guenter Ahlers[2] and Robert E. Ecke[1]

[1] Condensed-Matter & Thermal Physics and Center for Nonlinear Studies

Los Alamos National Laboratory, Los Alamos, NM 87545

[2] Department of Physics and Center for Nonlinear Sciences,

University of California, Santa Barbara, CA 93106

[3] Physikalisches Institut der Universität Bayreuth

95440 Bayreuth, Germany

(May 26, 1998)

Abstract

The Küppers-Lortz (KL) instability in Rayleigh-Bénard convection rotated about a vertical axis was studied experimentally using optical-shadowgraph imaging in the rotating frame for dimensionless rotation rates $6 < \Omega < 20$. Two cylindrical convection cells with radius-to-height ratios $, = 40$ and 23 were used. The cells contained CO_2 at 33.1 bar and 16.6 bar with Prandtl numbers $\sigma=0.93$ and $\sigma=0.83$, respectively. Numerical solutions of the Boussinesq equations with parameter values corresponding to the experiments were obtained for comparison. For $, = 40$ and $8 < \Omega < 10.5$, the initial pattern above onset was time dependent. Its dynamics revealed a mixture of sidewall-nucleated domain-wall motion characteristic of the KL instability and of dislocation-defect motion. For $\Omega > 10.5$, spontaneous formation of KL domain walls away from the sidewall was observed. For $8 < \Omega < 12$ there were differences between the two cells very close to onset, but for $\epsilon \gtrsim 0.02$

1